JM PAPERS

Stably stratified square cavity subjected to horizontal oscillations: responses to small amplitude forcing

Hezekiah Grayer II[1], **Jason Yalim**[1], **Bruno D. Welfert**[1] and **Juan M. Lopez**[1],†

[1]School of Mathematical and Statistical Sciences, Arizona State University, Tempe, AZ 85287, USA

A stably stratified fluid-filled two-dimensional square cavity is subjected to harmonic horizontal oscillations with frequencies less than the buoyancy frequency. The static linearly stratified state, which is an equilibrium of the unforced system, is not an equilibrium for any non-zero forcing amplitude. As viscous effects are reduced, the horizontally forced flows computed from the Navier–Stokes–Boussinesq equations tend to have piecewise constant or piecewise linear vorticity within the pattern of characteristic lines originating from the corners of the cavity. These flows are well described in the inviscid limit by a perturbation analysis of the unforced equilibrium using the forcing amplitude as the small perturbation parameter. At first order, this perturbation analysis leads to a forced linear inviscid hyperbolic system subject to boundary conditions and spatio-temporal symmetries associated with the horizontal forcing. A Fredholm alternative determines the type of solutions of this system: either the response is uniquely determined by the forcing, or it is resonant and corresponds to an intrinsic mode of the cavity. Both types of responses are investigated in terms of a waveform function satisfying a set of functional equations and are related to the behaviour of the characteristics of the hyperbolic system. In particular, non-retracing (ergodic) characteristics may lead to fractal responses. Models of viscous dissipation are also formulated to adjust the linear inviscid model for viscous effects obtained in the viscous nonlinear simulations.

Key words: stratified flows, parametric instability

1. Introduction

How a stratified body of fluid responds to external forcing depends on the geometry of the container, the boundary conditions and the nature of the forcing. While much insight has been gleaned from considering plane waves in unbounded stratified domains (Staquet &

† Email address for correspondence: juan.m.lopez@asu.edu

Sommeria 2002; Dauxois *et al.* 2018), physical observations necessarily involve flows in finite containers. Even small amplitude forcings can lead to large responses in confined systems with strong restoring forces such as Coriolis and buoyancy. The importance of parametric forcing and resonance in geophysical and astrophysical settings is well recognized (Le Bars, Cebron & Le Gal 2015); the point is that small amplitude mechanical forcings do not directly drive the large-scale flows but rather convert part of the available rotational and/or potential energies into intense fluid motions by resonating inertial and/or internal modes.

A classical example of parametric resonance is the Faraday wave problem (Faraday 1831), where standing waves on the surface of a liquid layer in a vertically oscillating container are formed. In the Faraday wave setting the parametric forcing is the oscillatory vertical acceleration of the container resulting in a vertically modulated gravity; typically a two-layer system is studied. The response to the parametric forcing manifests as surface or interfacial waves between the two layers of different density fluids, which may be immiscible or miscible. The experiments of Benielli & Sommeria (1998) explored vertical parametric forcing in a rectangular container, both with a two-layer system whose response was well described in terms of a system of Mathieu equations, and a continuously stratified fluid. The Mathieu equation describing a linear oscillator subject to parametric forcing is central to understanding Faraday waves (Benjamin & Ursell 1954; Miles & Henderson 1990; Kumar & Tuckerman 1994). In the continuously stratified case there was some correspondence with the two-layer responses, but not all. In the two-layer system they were able to experimentally identify the resonance tongues, whereas in the continuously stratified system they were not. Using numerical Floquet analysis of a temperature stratified analog of the Benielli & Sommeria (1998) continuously stratified experiment, the resonance tongues were clearly identified (Yalim, Lopez & Welfert 2018), and these results were used to calibrate viscous effects in a Mathieu model (Yalim, Welfert & Lopez 2019*a*). Nonlinear simulations showed complicated nonlinear dynamics near the edges of the resonance tongues, including subcritical behaviour to the low forcing frequency sides of the tongues (Yalim, Welfert & Lopez 2019*b*). Those numerical studies were in two dimensions, but Yalim, Lopez & Welfert (2020) showed that the complex nonlinear behaviour persists in three dimensions using a container with the same spanwise aspect ratio as used experimentally in Benielli & Sommeria (1998), until the forcing amplitude exceeded a level at which wave breaking ensues.

In Benielli & Sommeria (1998) the forced responses to vertical oscillations of the linearly stratified rectangular container correspond to resonantly excited modes of the container. When paddles or plungers are used to force such a rectangular container (e.g. Thorpe 1968; McEwan 1971), the response flow is a mix of modes with high regularity and beams with less regularity. More recent explorations have used increasingly more sophisticated semi-localized wave-makers to drive localized wavebeams (e.g. Mercier *et al.* 2010; Boury, Peacock & Odier 2019). These types of forcings inherently also include a component that is orthogonal to the direction of gravity. If the orthogonal component is small compared with the vertical accelerations then the response is largely that due to the vertical forcing, and remains well described by Mathieu equation models. On the other hand, there have been a number of studies where the parametric forcing is solely orthogonal to gravity, for the most part involving containers with a two-layer system oscillating horizontally (Wolf 1969, 1970; Wunenburger *et al.* 1999; Talib, Jalikop & Juel 2007; Jalikop & Juel 2009; Gaponenko *et al.* 2015; Shevtsova *et al.* 2016; Gréa & Briard 2019; Richter & Bestehorn 2019). In these horizontally oscillating systems a peculiar feature of the responses for some forcing frequencies is the saw-tooth shape of the surface, which remains invariant in the frame of the container, and is referred to as a frozen wave.

The vertically forced rectangular container with linear stable stratification has an equilibrium solution consisting of static fluid relative to the oscillating container. It is an equilibrium solution of the full nonlinear viscous problem for any forcing amplitude and frequency. The linearization of the governing equations about this state leads to a homogeneous Mathieu system describing deviations from this state, in which gravity modulation appears parametrically (i.e. multiplicatively). The trivial solution of the Mathieu system, consisting of zero perturbation velocity and zero temperature deviation away from linear stratification, is a solution for any forcing amplitude and frequency. The existence of non-trivial solutions in the Mathieu model determine a stability boundary in amplitude/frequency space (the edges of resonance tongues) where the trivial state becomes unstable. The instabilities correspond to resonantly excited eigenmodes of the unforced stratified cavity (Thorpe 1968). These resonant responses may be either synchronous or subharmonic with respect to the forcing.

In contrast, for the horizontally forced system, the static linearly stratified state is not a solution for any non-zero forcing amplitude, and so a Floquet analysis about that state is inappropriate. Instead, in the viscous nonlinear setting one needs to find the non-trivial responses at each point in parameter space. In the inviscid limit a perturbation analysis of the static linearly stratified state, using the small forcing amplitude as the perturbation variable, results at first order in a non-homogeneous linear system, where the gravity modulation appears as an external body force (i.e. additively). A similar perturbation analysis of the vertically forced system would lead to a trivial response at any order because the resulting effective gravity is a gradient term and simply modifies the pressure. The nature of the non-trivial response for the horizontally forced system depends on whether the frequency of the forcing is resonant or not. This can be codified in terms of the Fredholm alternative (Keller & Ting 1966), conveniently described in the context of finite-dimensional differential systems (Hale 2009): either the response is uniquely determined by the forcing, or it is resonant.

Responses obtained in stratified systems at the onset of instabilities also have strong similarities with those arising in rotating systems. In both cases, the linear inviscid limit leads to a Poincaré equation, a linear hyperbolic equation, for a perturbed temperature field (in the stratified case) or pressure field (in the rotating case). For confined systems, boundary conditions may lead to ill-posedness and a decrease in the regularity of solutions. Smooth solutions do exist and have been found via separation of variables in some geometries, such as a cylinder or a sphere in rotating systems (Kelvin 1880; Greenspan 1965) and in rectangular containers in stratified systems (Thorpe 1968; Turner 1979). Smooth intrinsic modes which are not completely separable have also been found, for example, in rotating rectangular containers (Maas 2003; Wu, Welfert & Lopez 2018b). However, one should in general expect singular (non-smooth) solutions (Aldridge 1975; Maas & Lam 1995; Rieutord, Georgeot & Valdettaro 2000; Harlander & Maas 2007; Swart *et al.* 2007; Bajars, Frank & Maas 2013; Borcia, Abouzar & Harlander 2014; Pillet *et al.* 2018; Rieutord & Valdettaro 2018; Wu, Welfert & Lopez 2020). These non-smooth solutions, which can be described as the superposition of an infinite number of regular 'modes' (and as such are non-separable), have been found in the inviscid limit in geometries where some or all of the container boundaries are neither parallel nor orthogonal to gravity or the mean rotation.

In continuously stratified systems viscosity can be quantified non-dimensionally in terms of a buoyancy number R_N, which is the ratio of the viscous time scale and buoyancy time scale. For small viscosity (large R_N) and small forcing amplitudes, the responses to horizontal oscillations at forcing frequencies (normalized by the buoyancy frequency) corresponding to ratios $r = n/m$, with m and n both odd integers, have mean enstrophy

several orders of magnitude larger than at any other frequency (corresponding to either irrational r or rational $r = n/m$ with m and n not both odd integers). The corresponding flow structure bears some resemblance to the eigenmodes of the unforced system at those frequencies, except that rather than being smooth, as was the case with the vertical forcing, the vorticity tends to be piecewise linear. The eigenmodes of the unforced system corresponding to frequencies associated to $r = n/m$ with m and n both odd integers are the only eigenmodes with spatio-temporal symmetry consistent with the horizontal forcing. At frequencies associated to $r = n/m$ with m and n having opposite parities, the response flows are not resonant and they tend to have piecewise constant vorticity as R_N is increased, with the constant regions delineated by the characteristics of the linear inviscid system emanating from the corners of the container. In contrast, the vertically forced flows are resonant at these frequencies. Other horizontal forcing frequencies result in response flows with further complications, including fractal patterns. By considering infinitesimal standing wave perturbations of the static linearly stratified state, we are able to solve the resulting non-homogeneous linear system analytically in the inviscid limit ($R_N \to \infty$) and recover virtually all the details of the nonlinear viscous response flows computed from the Navier–Stokes–Boussinesq equations with small viscosity (large, but finite R_N) and small forcing amplitudes. At the core of the analytic solution process lies a set of functional conditions obtained by imposing the symmetry and boundary conditions.

In this paper we consider the linearly stratified square container subjected to horizontal oscillations. The body force has a constant vertical component and an oscillatory horizontal component. In §2 the details of the problem and the governing equations are defined, their spatio-temporal symmetries are described, as is the numerical technique used for the nonlinear viscous problem. Section 3 describes these nonlinear viscous response flows at small forcing amplitudes and forcing frequencies covering the entire spectrum of the unforced system. As viscous effects are reduced (by increasing R_N), the response flows tend to have lower regularity with either piecewise constant or linear vorticity. These viscous nonlinear results are reconciled by considering the linear inviscid limit. This leads to a Poincaré equation for the temperature deviation. In §4 synchronous standing wave solutions to the Poincaré equation are found by exploiting the symmetries of the contained system. Several technical details pertaining to the analysis are presented in appendices. Section 5 provides a head-to-head comparison between the linear inviscid solutions and the nonlinear response flows at large but finite R_N and small forcing amplitudes. Finally, §6 summarizes and discusses potential implications for other forcing protocols, in particular, larger amplitude forcings, and the persistence of the results in three-dimensional (3-D) containers.

2. Governing equations, symmetries and numerics

Consider a fluid of kinematic viscosity ν, thermal diffusivity κ and coefficient of volume expansion β contained in a square cavity of side lengths L. The two vertical walls of the cavity are insulated and the two horizontal walls are held at fixed temperatures T_{hot} at the top and T_{cold} at the bottom, such that $\Delta T = T_{hot} - T_{cold} > 0$. Gravity g acts in the downward vertical direction. In the absence of any other external force, the fluid is linearly stratified. The non-dimensional temperature is $T = (T^* - T_{cold})/\Delta T - 0.5$, where T^* is the dimensional temperature. Length is scaled by L and time by $1/N$, where $N = \sqrt{g\beta\Delta T/L}$ is the buoyancy frequency. A Cartesian coordinate system $\boldsymbol{x} = (x, z) \in [-0.5, 0.5] \times [-0.5, 0.5]$ is attached to the cavity with its origin at the centre and the directions x and z aligned with the sides.

915 A85-4

$T = 0.5$

z

$\partial_x T = 0$ x $\partial_x T = 0$

$g_{eff} = -\alpha \sin \omega t \, \hat{e}_x - \hat{e}_z$

$T = -0.5$

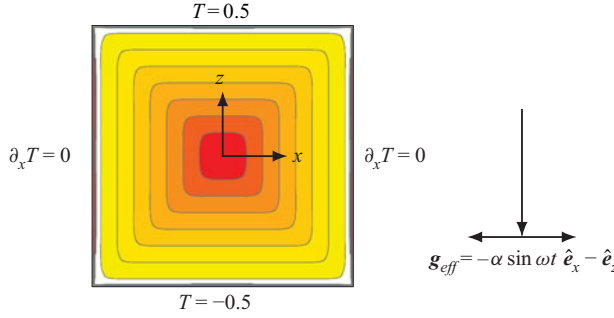Figure 1. Schematic of the stably stratified square cavity under harmonic horizontal forcing, together with the effective gravity vector g_{eff} relative to the horizontally oscillating cavity. A snapshot of the vorticity η is shown corresponding to buoyancy number $R_N = 10^6$, Prandtl number $Pr = 1$, forcing frequency $\omega = 0.71$ and forcing amplitude $\alpha = 1.75 \times 10^{-6}$.

The cavity is subjected to small harmonic horizontal oscillations of non-dimensional forcing frequency and amplitude ω and α. In the cavity reference frame the non-dimensional velocity is $\boldsymbol{u} = (u, w)$. The boundary conditions are no-slip on all walls for the velocity $\boldsymbol{u} = \boldsymbol{0}$. For the temperature, $T = \pm 0.5$ on the conducting walls at $z = \pm 0.5$ and $\partial_x T = 0$ on the insulated walls at $x = \pm 0.5$. Figure 1 shows a schematic of the system.

Under the Boussinesq approximation, the non-dimensional governing equations are

$$\left.\begin{aligned}
\partial_t u + u \partial_x u + w \partial_z u &= -\partial_x p + \frac{1}{R_N} \nabla^2 u + \alpha T \sin \omega t, \\
\partial_t w + u \partial_x w + w \partial_z w &= -\partial_z p + \frac{1}{R_N} \nabla^2 w + T, \\
\partial_t T + u \partial_x T + w \partial_z T &= \frac{1}{Pr R_N} \nabla^2 T, \\
\partial_x u + \partial_z w &= 0,
\end{aligned}\right\} \quad (2.1)$$

where p is the pressure, $Pr = \nu/\kappa$ is the Prandtl number and the buoyancy number $R_N = NL^2/\nu$ is the ratio of the viscous and buoyancy time scales (it is the square root of the Grashof number). The buoyancy number R_N can also be viewed as a ratio of a Reynolds number $u'L/\nu$ and Froude number u'/NL, where u' is a characteristic velocity, i.e. $(u'L/\nu)/(u'/NL) = NL^2/\nu = R_N$ (Riley & Lelong 2000). For the most part, we shall report on the temperature deviation, $\theta = T - z$, rather than on T itself.

For linearly stratified fluid in a rectangular container, if the boundary conditions on the horizontal walls for the stratifying agent are of Dirichlet type, such as is the case for fixed temperature on those walls, then the static linearly stratified state is a stable equilibrium irrespective of the viscosity or the thermal diffusivity of the fluid. This is not the case for salt stratification as the appropriate horizontal wall boundary conditions are of Neumann type, corresponding to no salt flux through the walls. The equilibrium state in that case is static with uniform density. In the inviscid limit the static linearly stratified equilibrium state with Dirichlet horizontal wall boundary conditions has neutral (i.e. zero growth rate) modes with a dense but discrete spectrum, consisting of a set of intrinsic frequencies (eigenvalues) which, when normalized by the buoyancy frequency, are in the interval $0 < |\sigma_r| < 1$. Finite viscosity imparts negative growth rates to these modes, so that in order to have a sustained non-trivial response flow, a physical viscous system needs

915 A85-5

to be continuously forced. The values of r for the intrinsic modes depend on the aspect ratio of the rectangular container. In the case of the square studied here, the discrete set corresponds to rationals $r = n/m$. The slopes of the characteristics are $\pm r$. If r is rational the characteristics retrace, whereas if r is irrational the characteristics never retrace and are said to be ergodic.

The static linearly stratified state $(u_s, w_s, p_s, T_s) = (0, 0, z^2/2, z)$ is a solution of the unforced system, (2.1) with $\alpha = 0$, for any Pr and R_N. When subjected to horizontal oscillations of small amplitude α, the response is synchronous with the forcing at frequency ω and has discrete time translation invariance

$$\mathcal{T} : [u, w, p, \theta](x, z, t) \mapsto [u, w, p, \theta](x, z, t + \tau), \tag{2.2}$$

where $\tau = 2\pi/\omega$ is the forcing period. The system is also invariant to two half-period-flip space–time symmetries $\mathcal{H}_x$ and $\mathcal{H}_z$, whose actions are

$$\mathcal{H}_x : [u, w, p, \theta](x, z, t) \mapsto [-u, w, p, \theta](-x, z, t + \tau/2), \tag{2.3}$$

$$\mathcal{H}_z : [u, w, p, \theta](x, z, t) \mapsto [u, -w, p, -\theta](x, -z, t - \tau/2). \tag{2.4}$$

The two symmetries $\mathcal{H}_x$ and $\mathcal{H}_z$ combine into a centrosymmetry $\mathcal{C} = \mathcal{H}_x\mathcal{H}_z = \mathcal{H}_z\mathcal{H}_x$, corresponding to a reflection through the origin, whose action is

$$\mathcal{C} : [u, w, p, \theta](x, z, t) \mapsto [-u, -w, p, -\theta](-x, -z, t). \tag{2.5}$$

The governing equations are solved numerically using a spectral-collocation method. It is the same technique as was used in Wu, Welfert & Lopez (2018*a*), Yalim *et al.* (2019*b*), Grayer *et al.* (2020) and Yalim *et al.* (2020). Briefly, the velocity, pressure and temperature are approximated by polynomials of degree $n = 160$ for $R_N \leq 10^6$ and $n = 224$ for $R_N = 10^7$, associated with the Chebyshev–Gauss–Lobatto grid. A selection of results were 'spot tested' using $n = 600$ for $R_N = 10^7$ in order to confirm that the results using $n = 224$ are indeed converged. A fractional step improved projection method, based on a linearly implicit and stiffly stable second-order accurate scheme, is used to integrate in time with $315/\omega$ time steps (rounded to the nearest decade) per forcing period, corresponding to a target time step $\delta t = 2 \times 10^{-2}$. Here, we fix $Pr = 1$ and the forcing amplitude $\alpha = 1.75 \times 10^{-6}$, and consider variations in R_N and ω. The choice of small α is such that for the range of R_N considered, the response flow remains the primary response, invariant to the spatio-temporal symmetries $\mathcal{H}_x$ and $\mathcal{H}_z$.

3. Limit cycle responses to small amplitude forcing

We begin by broadly describing how the flow responds over a wide range of squared forcing frequencies, $0 < \omega^2 < 1$, covering the spectrum of the intrinsic modes, for several $R_N \in [10^2, 10^7]$. Figure 2(*a*) summarizes these results in terms of a Bode magnitude plot consisting of response curves using the time-averaged enstrophy in the container, $\langle \mathcal{E} \rangle_\tau$, as a measure of the relative strength of the response flow, where

$$\langle \mathcal{E} \rangle_\tau = \frac{1}{\tau} \int_0^\tau \int_{-0.5}^{0.5} \int_{-0.5}^{0.5} \eta^2 \, \mathrm{d}x \, \mathrm{d}z \, \mathrm{d}t, \tag{3.1}$$

$\eta = \partial_z u - \partial_x w$ is the vorticity and $\tau = 2\pi/\omega$ is the forcing period, and figure 2(*b*) for the phase lag φ between phases associated with maximal horizontal forcing and maximal vorticity at the centre of the cavity in the response flow. The results are presented in terms of ω^2 rather than ω as the responses have a certain symmetry around $\omega^2 = 1/2$,
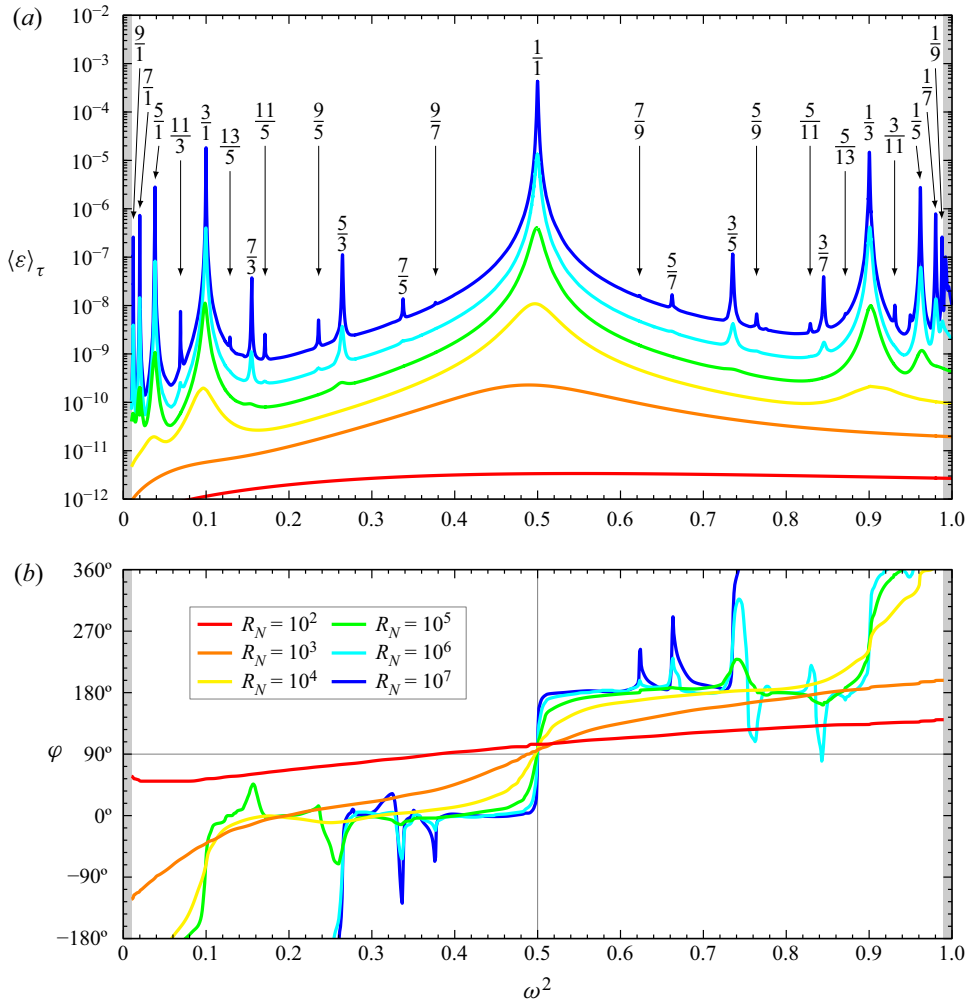
Figure 2. Bode plot, consisting of (*a*) magnitude response curves, $\langle \mathcal{E} \rangle_\tau$ vs. ω^2, and (*b*) phase lag response curves, φ vs. ω^2, for R_N as indicated. The rational values indicated are the ratios $r = n/m$ at squared frequencies $\omega^2 = 1/(1 + r^2)$.

which is detailed below. For the parameter ranges considered, all response flows are centrosymmetric limit cycles synchronous with the horizontal forcing.

Focusing on the squared forcing frequency range $0.45 < \omega^2 < 0.55$, which brackets the squared frequency $\omega^2 = m^2/(m^2 + n^2) = 1/2$ corresponding to the frequency of the primary intrinsic inviscid eigenmode with horizontal and vertical half-wavenumbers $m = n = 1$, the response is similar to that of a damped oscillator forced near its natural frequency. The magnitude and phase lag responses are almost flat at large damping (e.g. the $R_N = 10^2$ responses), and as R_N is increased, the magnitude response begins to show a broad increase preferentially near but below $\omega^2 = 1/2$, which sharpens and whose peak converges towards $\omega^2 = 1/2$ with increasing R_N. The phase lag response has an inflection point at the frequencies where the magnitude response has its peak, converging toward a step-function response as R_N is increased. The phase lag $\varphi \to 90°$ at $\omega^2 = 1/2$, $\varphi \to 0°$ for $\omega^2 < 1/2$, and $\varphi \to 180°$ for $\omega^2 > 1/2$. If the system were a simple damped

915 A85-7

spring–mass with a single natural frequency, this is all that would happen for forcing amplitudes that are not too large, but the unforced stratified cavity has natural frequencies $\sigma_r = m/\sqrt{m^2 + n^2} = 1/\sqrt{1 + r^2}$ for all rational values of $r = n/m$ (Thorpe 1968). For $R_N \leq 10^3$, all resonances are damped except for the $r = 1/1$ resonance just described. At $R_N = 10^4$, the magnitude response shows the development of peaks at frequencies corresponding to $r = 3/1$ and $r = 1/3$, as well as a weaker $r = 5/1$ peak. These, together with the $r = 1/5$ peak, sharpen with increasing R_N, much like the $r = 1/1$ peak. The phase lag behaviour is consistent with traversing through resonances, with the φ response curve developing inflection points near the resonating natural frequencies which develop into step functions as R_N is increased, with the step in φ being $180°$ across each resonance. As R_N is increased, more resonances are less damped and additional peaks become evident in the magnitude and phase lag responses. At $R_N = 10^7$, these peaks are identified in figure 2(a) by the rationals $r = n/m$, and the phase lag response only has inflections at these frequencies. If R_N is not sufficiently large for a particular resonance, there may only be a very slight peak in the magnitude response and the phase response does not change by $180°$ across the resonance but instead changes slightly and returns back to the phase lag on the other side of the resonance. Only the rationals $r = n/m$ with m and n both odd integers are resonated. These correspond to intrinsic modes whose spatio-temporal symmetries are compatible with those of the horizontal forcing, $\mathcal{H}_x$ and $\mathcal{H}_z$.

Figures 3 and 4 show snapshots of η and θ for various ω and R_N at phases of the forcing where η at the origin and θ are maximal (note that the maxima in η and θ are a quarter period out of phase). The supplementary movies 1 and 2 (available at https://doi.org/10.1017/jfm.2021.73) show animations of these over one forcing period. All cases shown in the movies are synchronous with the horizontal forcing, so that the phase lags for each case are easy to visualize.

When R_N is small, such as $R_N = 10^2$, the response flow across the whole frequency range is a single-cell limit cycle, somewhat reminiscent of the $1:1$ intrinsic eigenmode with squared eigenfrequency $\sigma_1^2 = 0.5$. As R_N is increased, the response flow tends to appear less smooth with either piecewise constant or piecewise linear vorticity, depending on the forcing frequency. For example, for $\omega^2 = 1/(1 + r^2)$ with $r = 1/1, 1/3$ and $3/1$ (i.e. $\omega^2 = 0.5, 0.9$ and 0.1), the vorticity of the response flows consists of one cell or three cells lined up either vertically or horizontally, with piecewise linear segments delimited by lines that start and end at the four corners of the cavity, reflecting a finite number of times on the walls, and whose slopes $\pm r$ correspond to the characteristics of the linear inviscid problem. For $\omega^2 = 0.8$ and 0.2, corresponding to $r = 1/2$ and $r = 2/1$, the response vorticity is piecewise constant with the pieces again being delimited by lines starting and ending at the four corners with slopes $\pm r$. The supplementary movies 1 and 2 show that for these rational values of r, the response flows are standing waves. For $\omega^2 = 0.3$ and 0.7, the corresponding $r = \sqrt{7/3}$ and $\sqrt{3/7}$ are irrational and inviscid characteristic lines starting from corners do not return to corners after a finite number of reflections, although they may get arbitrarily close to the corners. Even at $R_N = 10^7$, viscous dissipation and detuning effects are still present. For other irrational values of r, such as $\omega^2 = 0.3$ with $r = \sqrt{7/3}$ and $\omega^2 = 0.6$ with $r = \sqrt{2/3}$, the limit cycle response is not a standing wave. From the vorticity response, it appears that the flow at ω^2 corresponds to that at $1 - \omega^2$ with the vertical and horizontal directions interchanged, but this is not the case for the temperature deviation response.

Figure 5 provides a further quantitative demonstration of the piecewise low-degree polynomial (spline) nature of the vorticity and temperature deviation. It shows the profiles at $z = 0$ of the $\omega^2 \geq 0.5$ responses for the four largest values of R_N used.

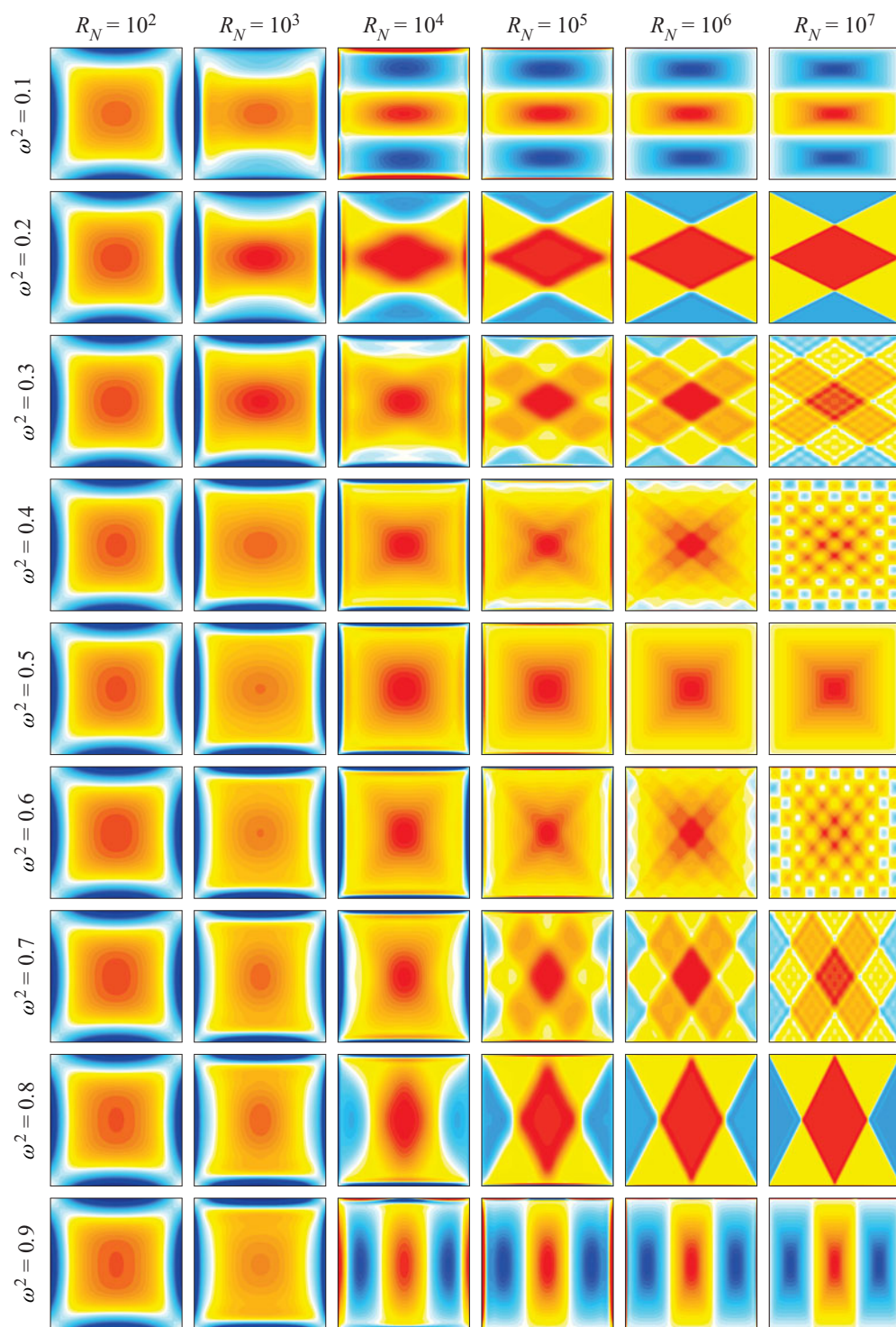## Stratified cavity subjected to horizontal oscillations

Figure 3. Snapshots of the vorticity η at indicated ω^2 and R_N, at times when η at the origin is maximal. The supplementary movie 1 animates these response flows over one forcing period.
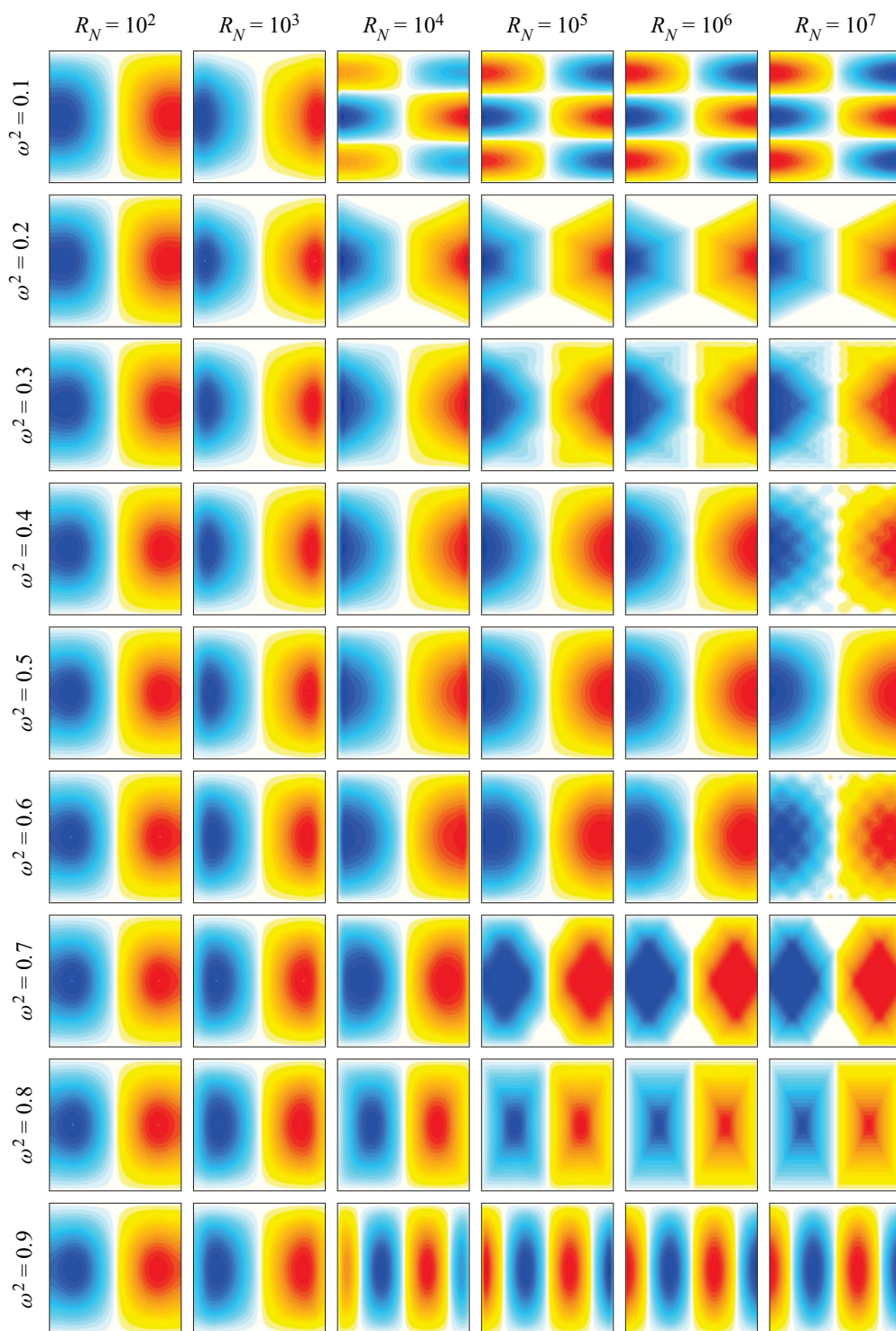
Figure 4. Snapshots of the temperature deviation θ at indicated ω^2 and R_N, at times corresponding to a quarter period after η is maximal at the origin. The supplementary movie 2 animates these response flows over one forcing period.
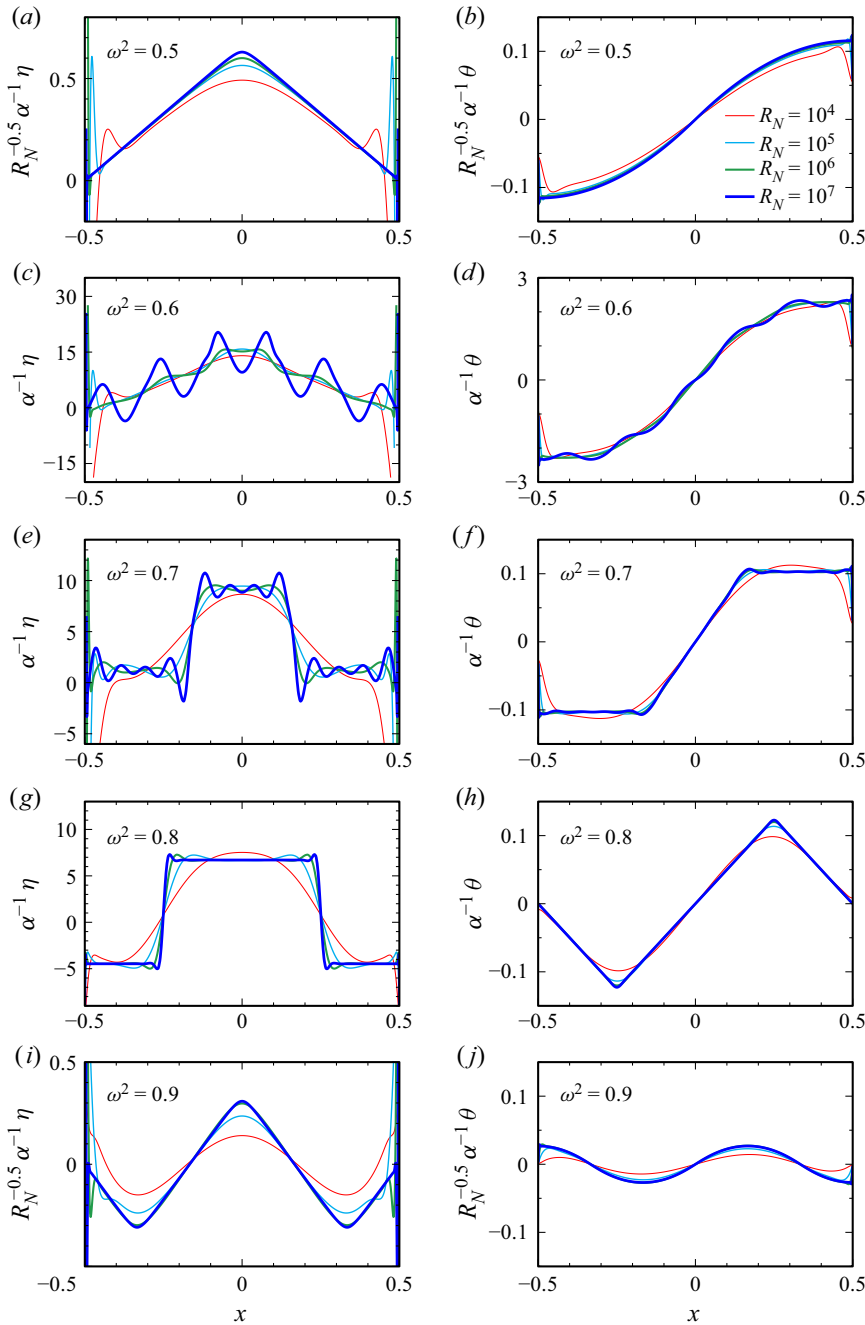
915 A85-10

Figure 5. Horizontal profiles at $z = 0$ of the vorticity η and temperature deviation θ from selected snapshots from figures 3 and 4 at ω^2 and R_N as indicated.

Several observations are in order: (i) the vorticity (shown in figure 5a,c,e,g,i), being a derived quantity obtained from the velocity components u and w, is in general less regular than the temperature deviation (shown in figure 5b,d,f,h,j); (ii) for $\omega^2 = 0.8$, both the vorticity and temperature profiles scale with the forcing amplitude α^{-1} and converge with

915 A85-11

increasing R_N towards piecewise constant and linear functions of the horizontal coordinate x, respectively; (iii) for $\omega^2 = 0.5$ or 0.9, corresponding to peaks in the response diagram (figure 2), the convergence with R_N requires additional scaling with a factor $R_N^{-0.5}$; (iv) for $\omega^2 = 0.7$, the vorticity profile exhibits oscillations in the vicinity of the 'jumps', and the temperature deviation also has oscillations at those locations; (v) for $\omega^2 = 0.6$, new features appear with increasing R_N, with large oscillations in the vorticity profile as well as noticeable oscillations in the temperature deviation profile.

While the jumps in the $\omega^2 = 0.7$ case are reminiscent of artifacts due to the Gibbs phenomenon in the spectral approximation of discontinuous functions (Tadmor 2007), the sheer size of the oscillations cannot be solely accounted for by such effects, which are known to be limited to approximately 9 % of the jump at a discontinuity. Increasing the numerical resolution does not change these profiles (at the respective values of R_N). This is contrary to what is expected of Gibbs oscillations, which become more localized with increased resolution, due to pointwise convergence away from jumps. The inviscid analysis carried out in the next section reconciles all the nonlinear viscous responses at large R_N and sheds light on the above observations, in particular, the general low regularity of solutions and the property that, in this problem, the response flows seem to exhibit finer-scale features at certain forcing frequencies when viscous effects are reduced.

4. Weak responses in the inviscid limit

The responses to horizontal forcing appear to be standing waves with less regularity than those observed in the case of purely vertical oscillatory forcing studied in Yalim *et al.* (2018). Here, we show how the responses to horizontal forcing can be constructed in the inviscid limit via a first-order perturbation analysis of the static linearly stratified state, using the forcing amplitude α as the small parameter. Specifically, in the inviscid limit ($R_N \to \infty$), using α as the small perturbation parameter and neglecting terms of order α^2 and higher, the equations describing the evolution of deviations (u, w, p, θ) away from (u_s, w_s, p_s, T_s) are

$$
\left.
\begin{aligned}
\partial_t u &= -\partial_x p + z\alpha \sin \omega t, \\
\partial_t w &= -\partial_z p + \theta, \\
\partial_t \theta &= -w, \\
\partial_x u + \partial_z w &= 0,
\end{aligned}
\right\}
\tag{4.1}
$$

subject to Dirichlet boundary conditions $u(\pm 0.5, z) = w(x, \pm 0.5) = \theta(x, \pm 0.5) = 0$. Note that the term $z\alpha \sin \omega t$ appearing in (4.1) cannot be absorbed into the pressure gradient in the form of a modified pressure. This results in a non-homogeneous (forced) linear system (4.1), whose general solution consists of the general solution to the homogeneous (unforced, $\alpha = 0$) system plus a particular solution. For $\omega^2 \neq 1$, a particular solution is

$$
\begin{bmatrix} u_p \\ w_p \end{bmatrix} = \frac{\alpha}{1 - \omega^2} \begin{bmatrix} 0 \\ -x\omega \end{bmatrix} \cos \omega t, \quad \begin{bmatrix} p_p \\ \theta_p \end{bmatrix} = \frac{\alpha}{1 - \omega^2} \begin{bmatrix} xz(1 - \omega^2) \\ x \end{bmatrix} \sin \omega t. \tag{4.2a,b}
$$

Eliminating u, w and p from (4.1) leads to the Poincaré equation (Poincaré 1885)

$$
\partial_{tt}(\partial_{xx} + \partial_{zz})\theta + \partial_{xx}\theta = 0, \tag{4.3}
$$

which is independent of the forcing amplitude α.

We now consider synchronous standing wave solutions of the form

$$\theta_h = [f(x + rz) + g(x - rz)] \sin \sigma_r t, \tag{4.4}$$

with arbitrary waveform functions f and g (that may depend on $r > 0$) and frequency σ_r satisfying the dispersion relation

$$\sigma_r^2 = 1/(1 + r^2) \quad \text{with } 0 < \sigma_r^2 < 1. \tag{4.5}$$

Note that the waveform functions f and g need only be defined for arguments in the interval $[-(1 + r)/2, (1 + r)/2]$.

Solutions to the homogeneous system are obtained by substituting (4.4) into (4.1) and setting $\alpha = 0$, i.e.

$$\left.\begin{aligned}
\begin{bmatrix} u_h \\ w_h \end{bmatrix} &= \begin{bmatrix} r\sigma_r[f(x + rz) - g(x - rz)] \\ -\sigma_r[f(x + rz) + g(x - rz)] \end{bmatrix} \cos \sigma_r t, \\
\begin{bmatrix} p_h \\ \theta_h \end{bmatrix} &= \begin{bmatrix} \lambda_r[F(x + rz) - G(x - rz)] \\ f(x + rz) + g(x - rz) \end{bmatrix} \sin \sigma_r t,
\end{aligned}\right\} \tag{4.6}$$

where $\lambda_r = r\sigma_r^2 = r/(1 + r^2)$, $F' = f$, $G' = g$ and $(\cdot)'$ denotes differentiation with respect to the argument. The system (4.1) forced at frequency $\omega = \sigma_r$ thus admits synchronous responses

$$\left.\begin{aligned}
\begin{bmatrix} u \\ w \end{bmatrix} = \begin{bmatrix} u_p + cu_h \\ w_p + cw_h \end{bmatrix} &= \begin{bmatrix} cr\sigma_r[f(x + rz) - g(x - rz)] \\ -\alpha x/(r^2\sigma_r) - c\sigma_r[f(x + rz) + g(x - rz)] \end{bmatrix} \cos \sigma_r t, \\
\begin{bmatrix} p \\ \theta \end{bmatrix} = \begin{bmatrix} p_p + cp_h \\ \theta_p + c\theta_h \end{bmatrix} &= \begin{bmatrix} \alpha xz + c\lambda_r[F(x + rz) - G(x - rz)] \\ \alpha x/(r^2\sigma_r^2) + c[f(x + rz) + g(x - rz)] \end{bmatrix} \sin \sigma_r t,
\end{aligned}\right\} \tag{4.7}$$

for any constant c, where the identity $1/(1 - \omega^2) = 1/(1 - \sigma_r^2) = 1/(r^2\sigma_r^2)$ has been used. The streamfunction ψ, whose gradient is $(\partial_x\psi, \partial_z\psi) = (-w, u)$, and the vorticity $\eta = \partial_z u - \partial_x w$ of these responses are

$$\begin{bmatrix} \psi \\ \eta \end{bmatrix} = \begin{bmatrix} \alpha x^2/(2r^2\sigma_r) + c\sigma_r[F(x + rz) + G(x - rz)] \\ \alpha/(r^2\sigma_r) + (c/\sigma_r)[f'(x + rz) + g'(x - rz)] \end{bmatrix} \cos \sigma_r t. \tag{4.8}$$

The linear system (4.1) has the same spatio-temporal symmetries, $\mathcal{H}_x$ and $\mathcal{H}_z$, as the full Navier–Stokes system (2.1). For $c \neq 0$, these symmetries imply, for all $|x| \leq 0.5$ and $|z| \leq 0.5$ (i.e. everywhere inside the container), that

$$f(\mp x \pm rz) - g(\mp x \mp rz) = \pm f(x + rz) \mp g(x - rz), \tag{4.9a}$$

$$f(\mp x \pm rz) + g(\mp x \mp rz) = \mp f(x + rz) \mp g(x - rz). \tag{4.9b}$$

Adding (4.9a) and (4.9b) shows that $f = g$ and that both waveform functions are odd. The resulting u in (4.7) is even in x and odd in z, w and θ are odd in x and even in z, while p is odd in both x and z, and ψ and η are both even in x and z.

In general, the imposition of boundary conditions on the Poincaré equation (4.3) leads to ill-posedness, with no solution when it is overspecified or multiple solutions if it is underspecified. The condition $u(0.5, z, t) = 0$ constraints f to be even around 0.5,

$$f(0.5 + \zeta) = f(0.5 - \zeta), \quad \text{where } |\zeta| \leq r/2 \text{ and } \zeta = rz, \tag{4.10}$$

while the boundary condition $w(x, 0.5, t) = 0$ requires

$$f(x + r/2) + f(x - r/2) = -\alpha x/(cr^2\sigma_r^2), \quad |x| \leq 0.5. \tag{4.11}$$

The following Fredholm alternative then holds for the waveform function f:

A1: either $c = c_r = -\alpha/(2r^2\sigma_r^2) = -\alpha/(2r\lambda_r)$ is finite and f satisfies the functional equation

$$f(x + r/2) + f(x - r/2) = 2x, \quad |x| \leq 0.5; \quad (4.12)$$

A2: or, $c = \infty$ and f is even around $r/2$,

$$f(r/2 + x) = -f(x - r/2) = f(r/2 - x), \quad |x| \leq 0.5. \quad (4.13)$$

The Fredholm alternative is a classical tool describing the existence of solutions of non-homogeneous linear equations; see Hale (2009) for a description in the differential equations context. Here, the alternative **A2** is similar to case (A) in theorem 3 of Swart *et al.* (2007), corresponding to multiple solutions defined up to a scaling factor. The three conditions, (4.10), f odd, and either of (4.12) or (4.13), form systems of functional equations of the Schröder or Abel type (Kuczma, Choczewski & Ger (1990), § 3.5). The relevance of these types of equations to confined stratified flows was originally recognized by Manton & Mysak (1971), and later exploited by Beckebanze (2015) and Beckebanze & Keady (2016) to obtain exact inviscid solutions with low regularity properties in a stratified trapezoidal channel. One major complication in the flows presently under consideration, compared with that considered in Beckebanze (2015), is due to the forcing term in (4.1). Although this term does not affect the Poincaré equation (4.3), it changes the type of the resulting condition, from a (non-homogeneous/forced) Abel equation (4.12) to a (homogeneous/unforced) Schröder equation (4.13).

In the remainder of this section we describe solutions that are obtained for different values of r. For the square cavity considered here, the nature of the solutions depends on whether or not r is rational, i.e. whether the characteristic lines emanating from the corners of the cavity, $x \pm rz = \pm 0.5(1 \pm r)$, retrace or not. Furthermore, when r is rational, the nature of the solutions depends on the parities of the integers m and n in the irreducible representation of $r = n/m$ (greatest common denominator $\gcd(m, n) = 1$). Since the waveform function f is determined from conditions that depend on r, we shall use the notation f_r instead of f when referring to a specific value of r, with a resulting response flow $(u_r, w_r, p_r, \theta_r)$.

4.1. *Alternative A1: forced responses*

There is a relationship between the solutions of (4.1) at squared forcing frequency $\omega^2 = \sigma_r^2 = 1/(1 + r^2)$, associated with waveform function f_r, and those at $1 - \sigma_r^2 = r^2/(1 + r^2) = 1/(1 + (1/r)^2)$, associated with $f_{1/r}$. The details are provided in Appendix A. It is therefore sufficient to consider $r \in (0, 1)$, i.e. $\sigma_r^2 \in (1/2, 1)$.

First, we identify waveform functions f_r satisfying (4.12) for selected rational values $r = n/m$ with $m > n$. Evaluating (4.12) at $x = [x_j]_{1 \leq j \leq m}$ with $x_j = j/(2m)$, $j = 1, \ldots, m$, and using the symmetries approximately 0 (f_r odd) and 1/2 (4.10), yields an $m \times m$ linear system in $\boldsymbol{f}_r(\boldsymbol{x}) = [f_r(x_j)]_{1 \leq j \leq m}$,

$$\boldsymbol{A}\boldsymbol{f}_r(\boldsymbol{x}) = 2\boldsymbol{x}. \quad (4.14)$$

Harlander & Maas (2007) derived a similar system using a boundary collocation approach for the solution of the Poincaré equation in two-dimensional (2-D) containers.

When m and n have opposite parities, this system is non-singular and has a unique solution $\boldsymbol{f}_r(\boldsymbol{x})$. The construction of the system and its solution is illustrated in Appendix B for the case with $m = 11$ and $n = 4$. The linear spline obtained by connecting the points
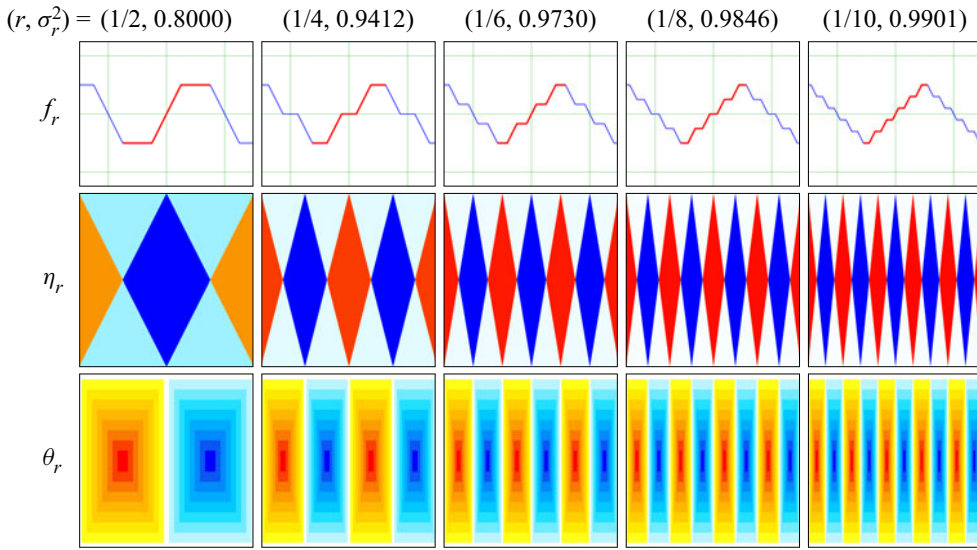
915 A85-14

Figure 6. Waveform function f_r in $[-1.5, 1.5] \times [-1.25, 1.25]$ and the associated scaled forced responses η_r at phase 0 and θ_r at phase $\pi/2$, from (4.15) at r as indicated. The blue curve is the 2-periodic extension of the red curve f_r defined in the interval $[-(1+r)/2, (1+r)/2]$.

$[x_j, f_r(x_j)]$ satisfies (4.10) and (4.12) for all $x \in [-(1+r)/2, (1+r)/2]$. This solution f_r is plotted in red in the first row of figure 6 for the cases $n = 1$ and $m = 2, 4, 6, 8$ and 10. A unique 2-periodic extension, obtained by enforcing (4.10) and $f_r(-\zeta) = -f_r(\zeta)$ for all real ζ, is shown in blue. This extension satisfies $f_r(\pm 1) = 0$. Note that additional periodic extensions exist for $0 < r < 1$, $[-(1+r)/2, (1+r)/2] \subset [-1, 1]$.

The value of the waveform function f_r in $[-(1+r)/2, (1+r)/2]$ completely determines the response flow of the forced linear system (4.1) everywhere in the square cavity. This response flow is

$$
\left.
\begin{aligned}
\begin{bmatrix} u_r \\ w_r \end{bmatrix} &= c_r \sigma_r \begin{bmatrix} r[f_r(x+rz) - f_r(x-rz)] \\ 2x - f_r(x+rz) - f_r(x-rz) \end{bmatrix} \cos \sigma_r t, \\
\begin{bmatrix} p_r \\ \theta_r \end{bmatrix} &= -c_r \begin{bmatrix} \lambda_r[2rxz - F_r(x+rz) + F_r(x-rz)] \\ 2x - f_r(x+rz) - f_r(x-rz) \end{bmatrix} \sin \sigma_r t.
\end{aligned}
\right\}
\tag{4.15}
$$

Its magnitude is linearly proportional to the forcing amplitude α.

The forced response (4.15) is now considered for three different sequences of rationals $r = n/m$ with n and m of opposite parities, which converge to $r = 0$, $r = 1/\sqrt{2}$ (an irrational number) and $r = 1$. These sequences reveal qualitatively different behaviours.

The vorticity η_r and temperature deviation θ_r for the sequence $r = 1/m$, $m = 2, 4, 6, \ldots$ converging to $r = 0$, associated with $\sigma_r^2 = 1/(1 + r^2) = 1$, are illustrated in figure 6 for the first five cases $m = 2, 4, 6, 8$ and 10. For $r = 1/2$, η_r is piecewise constant with the pieces delimited by the characteristic lines emanating from the corners forming a pattern known as a harlequin print, and θ_r is piecewise linear in the form of two pyramids, one positive and the other negative, either side of $x = 0$. As the even integer m increases, the 2-periodic extension of f_r looks more and more like a triangular wave with $f_r(x) = x$ for $|x| \leq 0.5$ and the response flows consist of $m/2$ copies of the $r = 1/2$ response with $x \to (m/2)x$.
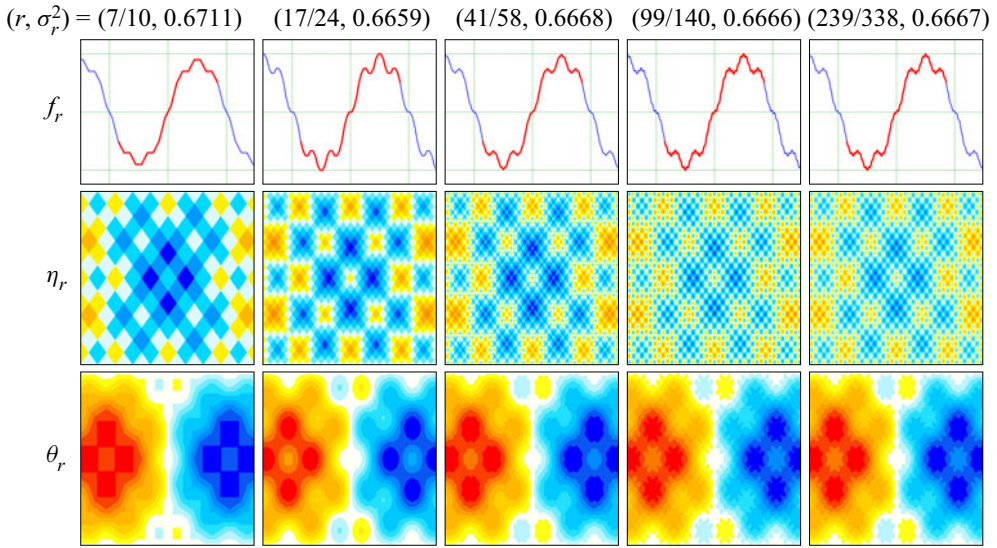
$(r, \sigma_r^2) = (7/10, 0.6711)$ $(17/24, 0.6659)$ $(41/58, 0.6668)$ $(99/140, 0.6666)$ $(239/338, 0.6667)$

Figure 7. Waveform function f_r in $[-1.5, 1.5] \times [-1.25, 1.25]$ and associated scaled forced responses η_r at phase 0 and θ_r at phase $\pi/2$ for a series of rational r values converging to the irrational $1/\sqrt{2}$, corresponding to $\sigma_r^2 = 2/3$. The blue curve is the 2-periodic extension of the red curve f_r defined in the interval $[-(1 + r)/2, (1 + r)/2]$.

We now consider a sequence of rationals $r = n/m$ with m and n of opposite parities, converging to the irrational value $r = 1/\sqrt{2}$, corresponding to $\sigma_r^2 = 1/(1 + r^2) = 2/3$. Such a sequence can be obtained from successive partial sums of the continued fraction representation

$$\frac{1}{\sqrt{2}} = \frac{\sqrt{2}}{2} = \frac{1}{2}\left[1 + \cfrac{1}{2 + \cfrac{1}{2 + \cdots}}\right], \tag{4.16}$$

according to the iteration $r \to (1 + r)/(1 + 2r)$, starting with the case $r = 1/2$. Figure 7 shows the waveform function f_r and the associated response η_r and θ_r for five consecutive iterates of r. The value $f_r(1/2)$ is observed to rapidly approximate 1 as $r \to 1/\sqrt{2}$, with f_r exhibiting increasingly higher frequency spatial variations, and finer and finer structure in the corresponding η_r and θ_r. The curve $f_{1/\sqrt{2}}$, obtained at the limit $r = 1/\sqrt{2}$, appears to be fractal.

Figure 8 shows f_r and η_r at a rational value of r approximating $1/\sqrt{2}$, obtained from the fourteenth iterate of the sequence. The figures appear qualitatively similar to lower iterates shown in figure 7; the higher iterates allow us to zoom-in and explore the fractal nature of the response in the limit $r \to 1/\sqrt{2}$, from which the similarity relation

$$f_r(0.5s + [1 - s]x) = s f_r(0.5) + [1 - s] f_r(x), \tag{4.17}$$

with $s = 2r/(1 + r) = 2\sqrt{2} - 2 \approx 0.828$, can be inferred. The relation (4.17), equivalent to

$$\begin{bmatrix} \zeta \\ f_r(\zeta) \end{bmatrix} = \begin{bmatrix} 0.5 \\ f_r(0.5) \end{bmatrix} + (1 - s)\begin{bmatrix} x - 0.5 \\ f_r(x) - f_r(0.5) \end{bmatrix}, \tag{4.18}$$
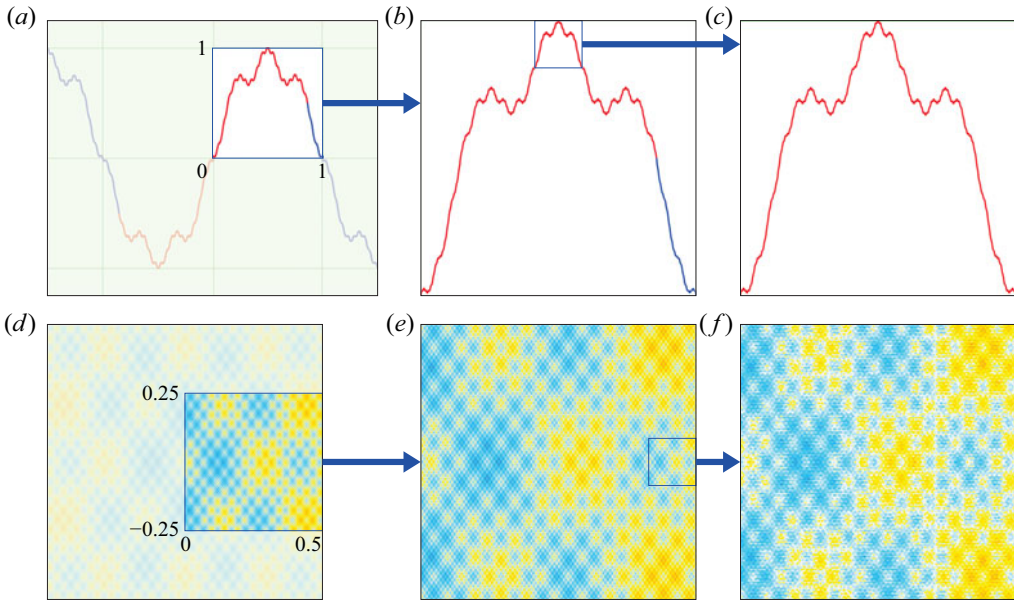
Figure 8. Zoom-in in the neighbourhood of $(0.5, 0)$ for η_r at phase 0; (*a*–*c*) waveform function $f_{1/\sqrt{2}}$ in windows $[-1.5, 1.5] \times [-1.25, 1.25]$ (*a,d*), $[0, 1] \times [0, 1]$ (*b,e*) and $[s/2, 1 - s/2] \times [s, 1]$ (*c,f*) with $s = 2\sqrt{2} - 2$; (*d*–*f*) η_r in regions $[-0.5, 0.5] \times [-0.5, 0.5]$ (square cavity; *a,d*), $[0, 1/2] \times [-1/4, 1/4]$ (*b,e*) and $[s/2, 1/2] \times [-(1 - s)/4, (1 - s)/4]$ (*c,f*). The supplementary movie 3 shows a continuous zoom-in of the response η_r about the point $(x, z) = (0.5, 0)$.

shows that the graph of $f_{1/\sqrt{2}}$ is invariant under the homothety with similarity factor $1 - s = 3 - 2\sqrt{2} \approx 0.172$ and centre $(0.5, f_{1/\sqrt{2}}(0.5)) = (0.5, 1)$. Figure 8 illustrates how the curve $f_{1/\sqrt{2}}$ in the range $[s/2, 1 - s/2]$, of size $1 - s$ centred around 0.5, is a scaled-down copy of itself from the range $[0, 1]$. The supplementary movie 3 shows a continuous zoom into the region in the neighbourhood of the point $(x, z) = (0.5, 0)$ of the response η_r shown in figure 8. The relation (4.17) is not trivial and can be verified to hold for other quadratic irrational values of r, with exactly the same definition of $s(r)$ when $r^2 = 1 - 1/m$, $m = 3, 4, \ldots$, and when $r^2 = 1 + 1/m$, $m = 1, 2, \ldots$, or with a modified rational relationship for other quadratic irrational values of r.

The third sequence of rationals considered is $r = n/m = (m - 1)/m = 1 - 1/m$, $m = 2, 3, 4, \ldots$ converging to $r = 1$, which is associated with $\sigma_r^2 = 1/(1 + r^2) = 1/2$. Figure 9 illustrates the behaviour of the solution of the functional equations, f_r, and the corresponding forced response η_r and θ_r. As m increases, the maximum value of $f_{1-1/m}$, which is attained at 0.5, increases unboundedly as $O(m) = O(1/(1 - r))$. As a consequence, the forced response also grows in magnitude as $m \to \infty$ and $r \to 1$, with the piecewise constant vorticity η_r showing a finer and finer harlequin pattern converging towards a piecewise linear vorticity profile in the shape of an inverted pyramid, and the temperature deviation θ_r converges towards a piecewise quadratic field with isocontours in the form of perfect (arcs of) circles centred at $(\pm 0.5, 0)$ and hyperbolas centred at $(0, \pm 0.5)$ meeting at the limiting characteristics $x \pm z = 0$; see figure 9. The unbounded response at the limit $r = 1$ corresponds to resonance, which is discussed below under the umbrella of the Fredholm alternative **A2**. The unbounded growth of the magnitude of the response being inversely proportional to the distance to the limiting critical frequency also conforms to the standard result from forced undamped mechanical linear oscillators.
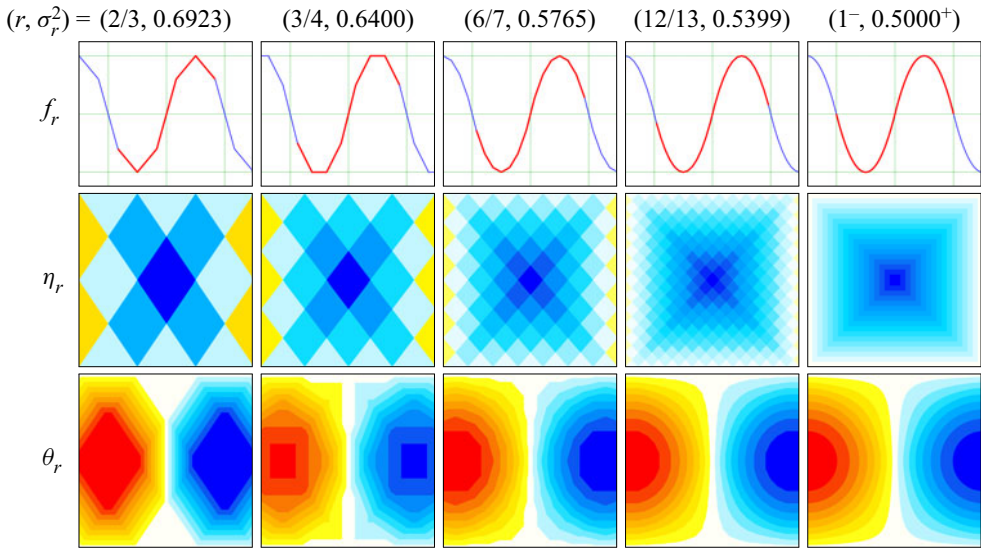
$(r, \sigma_r^2) = (2/3, 0.6923)$ $(3/4, 0.6400)$ $(6/7, 0.5765)$ $(12/13, 0.5399)$ $(1^-, 0.5000^+)$

Figure 9. Scaled waveform function f_r in $[-1.5, 1.5] \times [-1.25, 1.25]$ and the associated scaled forced responses η_r at phase 0 and θ_r at phase $\pi/2$ for a series of rational r values converging to $r = 1$, corresponding to $\sigma_r^2 = 1/2$. The blue curve is the 2-periodic extension of the red curve f_r defined in the interval $[-(1 + r)/2, (1 + r)/2]$.

4.2. *Alternative A2: intrinsic modes*

At exactly $r = 1$, the Fredholm alternative **A1** fails: the conditions $f(1) = f(0)$ ((4.10) with $\zeta = 0.5$) and $f(1) + f(0) = 1$ (alternative **A1** with $x = 0.5$) lead to a contradiction with $f(0) = 0$ (f odd). Equivalently, the system (4.14) reduces to the inconsistent single equation $[0]f(0.5) = 2[0.5]$. The inconsistency of the system (4.14) is also illustrated for $r = 3/5$ in Appendix B. In these cases, the Fredholm alternative **A2** must hold. For $r = 1$, alternative **A2** reduces to (4.10); for every odd waveform function $f = f(\zeta)$ which is even around $\zeta = 0.5$, there is a corresponding solution of the unforced homogeneous problem (4.1) constructed from (4.6). Examples of f that naturally satisfy these symmetry conditions include the family of shifted Euler splines $f(\zeta) = S_q(\zeta - 0.5)$, of regularity class C^{q-1}(Olver *et al.* (2010), (24.17.3)). These splines are defined from the Euler polynomials E_q (Olver *et al.* (2010), § 24). They are 1-antiperiodic (Olver *et al.* (2010), (24.2.12)) and, hence, 2-periodic. They also belong to the more general family of exponential Euler splines (Schoenberg (1973), Lecture 3, § 5). This family includes the C^0 linear triangular wave S_1, the C^1 quadratic spline S_2 defined by $S_2(\zeta - 0.5) = 4\zeta(1 - |\zeta|)$ for $|\zeta| \le 1$, and the C^∞ waveform function $f(\zeta) = \sin(\pi\zeta) = \lim_{q \to \infty} S_q(\zeta - 0.5)$. Figure 10 shows the structure of S_1, S_2, S_3 and S_∞; note the remarkable similarity between S_q for $q \ge 2$.

The choice $f_1(\zeta) = S_\infty(\zeta - 0.5) = \sin(\pi\zeta)$ leads to the C^∞ intrinsic mode

$$\left.\begin{array}{l} \begin{bmatrix} u_h \\ w_h \end{bmatrix} \propto \sigma_1 \begin{bmatrix} \cos \pi x \, \sin \pi z \\ -\sin \pi x \, \cos \pi z \end{bmatrix} \cos \sigma_1 t, \\[12pt] \begin{bmatrix} p_h \\ \theta_h \end{bmatrix} \propto \begin{bmatrix} (\lambda_1/\pi) \sin \pi x \, \sin \pi z \\ \sin \pi x \, \cos \pi z \end{bmatrix} \sin \sigma_1 t, \end{array}\right\} \tag{4.19}$$
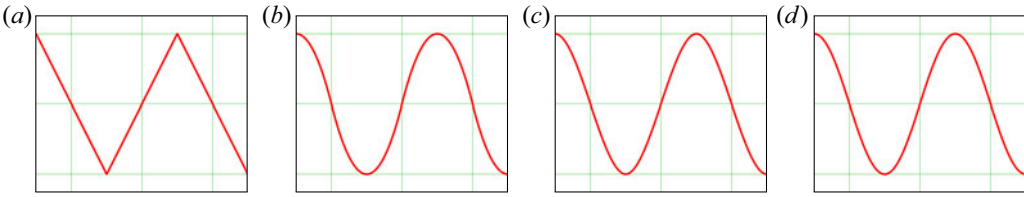
Figure 10. Shifted Euler splines S_q, of regularity class C^{q-1}, shown in a window $[-1.5, 1.5] \times [-1.25, 1.25]$: (*a*) $S_1(\zeta - 0.5) = E_1(\zeta + 0.5)/E_1(0) = 2\zeta$ for $-0.5 < \zeta < 0.5$, (*b*) $S_2(\zeta - 0.5) = E_2(\zeta)/E_2(0.5) = 4\zeta(1 - \zeta)$ for $0 < \zeta < 1$, (*c*) $S_3(\zeta - 0.5) = -E_3(\zeta + 0.5)/E_3(0) = \zeta(3 - 4\zeta^2)$ for $-0.5 < \zeta < 0.5$, and (*d*) $S_\infty(\zeta - 0.5) = \sin(\pi\zeta)$, where E_q is the Euler polynomial of degree q.

with $\sigma_1 = 1/\sqrt{2}$ and $\lambda_1 = 1/2$, which was shown to be excited by purely vertical forcing oscillations of the container (Yalim *et al.* 2018). In contrast, for the horizontal forcing considered here, the limit of the forced responses associated with the sequence $r = 1 - 1/m$ with $m \geq 2$ corresponds to the quadratic spline S_2. Specifically,

$$\lim_{m \to \infty} \frac{f_{1-1/m}(\zeta)}{f_{1-1/m}(0.5)} = 4\zeta(1 - |\zeta|) = S_2(\zeta - 0.5), \quad |\zeta| \leq 1; \tag{4.20}$$

see Appendix C for a proof. The eigenmode components η_1 and θ_1 are visually indistinguishable from the bottom row of figure 9, obtained for $r = 1 - 1/m$ with m large.

The resonance at $\omega^2 = 1/2$ (i.e. $r = 1$) corresponds to the largest peak in the Bode response diagram in figure 2(*a*). Similar resonances occur for all rational values $r = n/m$ with both m and n odd integers, leading to other peaks in the Bode diagram at the corresponding values of $\omega^2 = \sigma_r^2 = 1/(1 + r^2)$. These are all the cases for which Fredholm alternative **A2** holds. The scaling relation

$$f_{n/m}(\zeta) = f_1(m\zeta), \tag{4.21}$$

shown in Appendix D, implies that the resulting mode, denoted $M_{m:n}$, can be simply constructed from $M_{1:1}$, with vorticity and temperature deviation components η_r and θ_r arranged in a regular $m \times n$ tiling of the scaled components of $M_{1:1}$.

Figure 11 shows the vorticity η_r and temperature deviation θ_r for the eigenmode $M_{5:3}$ resonating at squared frequency $\sigma_r^2 = 25/34 \approx 0.7353$ (corresponding to $r = 3/5$). The response consists of an exact 5×3 tiling of copies of the components of the mode $M_{1:1}$, with piecewise linear η_1 in a pyramid pattern and piecewise quadratic θ_1. The responses at slightly detuned frequencies on either side (slightly smaller and larger values of r) of the resonant modal case are also shown. These forced responses, being associated with rational values of r that are approximations of the resonant case $r = 3/5$, have piecewise constant η_r and piecewise linear θ_r. At the macroscopic scale of the figure, they appear to be smooth with one order of regularity higher than they actually possess. This is due to the natural visual (Riemann) integration of the small scales associated with the underlying network of characteristic lines emanating from the corners, resulting from the large values of m and n in the irreducible representation of $r = n/m$. Whereas the eigenmode has velocity and temperature fields of regularity class C^1 and satisfies the homogeneous linear inviscid system (4.1) in a pointwise or strong sense, the forced response at a detuned frequency has velocity and temperature fields only of class C^0 globally, as a result of the nature of the forcing, and are weak solutions.

Note that the waveform functions f_r shown in figure 11 are normalized, with extrema at ± 1. In fact, the extrema of f_r are, as in the case at $r = 1$, unbounded at the
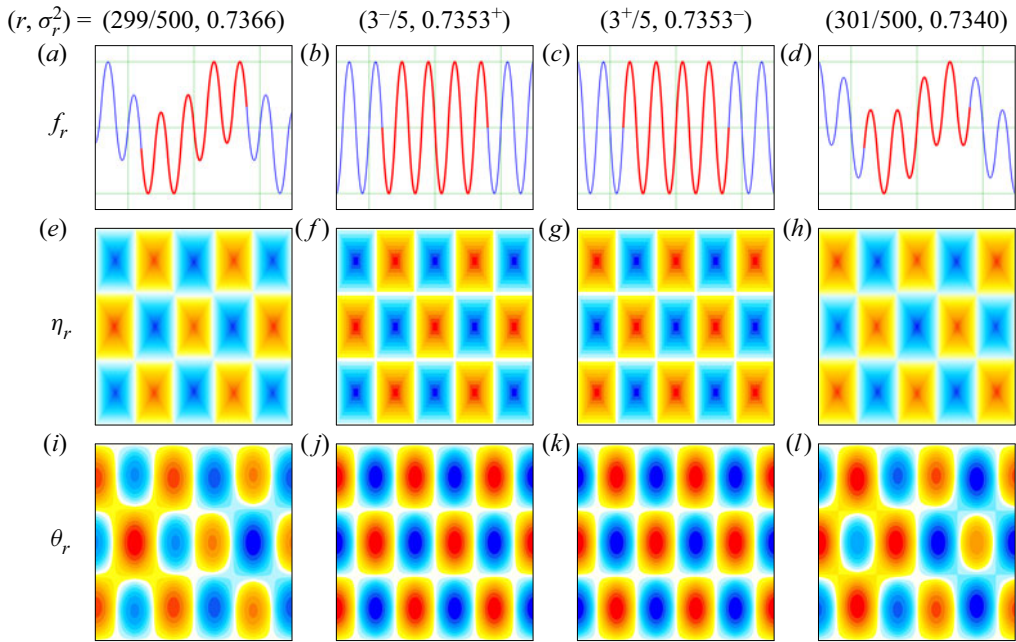
Figure 11. Scaled waveform function f_r in $[-1.5, 1.5] \times [-1.25, 1.25]$ and associated scaled forced response (η_r at phase 0 and θ_r at phase $\pi/2$) for two values $r = (300 \pm 1)/500$ close to $3/5$ (a,e,i,d,h,l) and eigenmode at $r = 3/5$ (b,f,j,c,g,k, associated with opposite scaling). The blue curve is the 2-periodic extension of the red curve f_r defined in the interval $[-(1 + r)/2, (1 + r)/2]$.

resonant frequency. As the forcing frequency is varied across the resonant frequency, there is an inversion $f_r \to -f_r$. At resonance, the intrinsic mode of the unforced system is given by

$$
\left.
\begin{aligned}
\begin{bmatrix} u_r \\ w_r \end{bmatrix} &= \sigma_r \begin{bmatrix} r[f_r(x + rz) - f_r(x - rz)] \\ -f_r(x + rz) - f_r(x - rz) \end{bmatrix} \cos \sigma_r t, \\
\begin{bmatrix} p_r \\ \theta_r \end{bmatrix} &= \begin{bmatrix} \lambda_r[F_r(x + rz) - F_r(x - rz)] \\ f_r(x + rz) + f_r(x - rz) \end{bmatrix} \sin \sigma_r t,
\end{aligned}
\right\}
\tag{4.22}
$$

obtained by letting $\alpha = 0$ in (4.7). So, the change in sign in f_r is equivalent to a half-period phase shift in time. This is evident from comparing figures 11(a–d) and 11(i–l). Interestingly, this shift occurs in the high spatial frequency component of f_r, not the low spatial frequency component. This shift is emphasized in figures 11(b,f,j) and 11(c,g,k), representing the eigenmode, scaled to ± 1 according to which side of the resonant frequency and the associated parameter $r = 3/5$ they correspond. Also note how the cellular grid modal pattern of the piecewise quadratic temperature deviation θ_r becomes distorted along the characteristic directions and the cells merge upon detuning away from the resonance.

4.3. *Spectral representations of modal and forced responses*

The visual similarity between the quadratic spline S_2 and the sine wave S_∞ in figure 10 can be quantified via the sine Fourier series expansion (Olver *et al.*
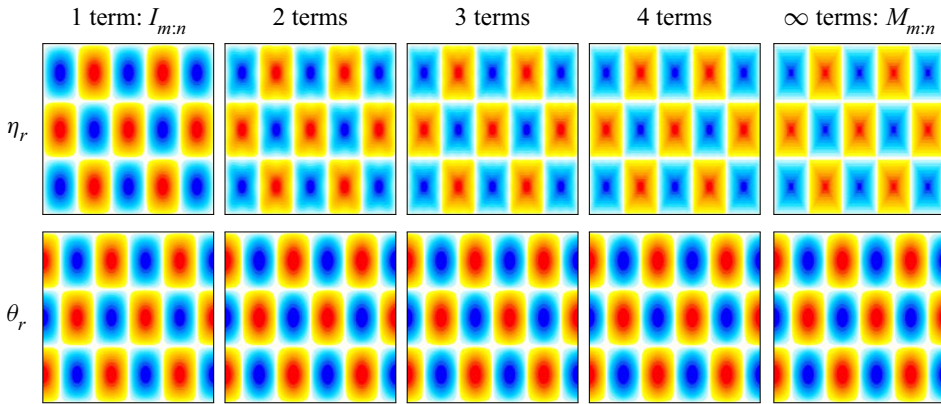
Figure 12. Plots of the vorticity η_r and temperature deviation θ_r associated with the partial sums in the series expansion of $M_{5:3}$ in (4.24), for the number of indicated terms.

2010, (24.8.4))

$$S_2(\zeta - 0.5) = \frac{32}{\pi^3} \sum_{k \geq 0} \frac{\sin(2k+1)\pi\zeta}{(2k+1)^3} = \frac{32}{\pi^3} \left[S_\infty(\zeta - 0.5) + \frac{1}{3^3} S_\infty(3\zeta - 0.5) + \dots \right].$$
(4.23)

By approximating the factor $32/\pi^3 \approx 1.032 \approx 1$ in (4.23), the resonating mode $M_{m:n}$ can be expanded as a superposition of an infinite number of C^∞ intrinsic modes $I_{(2k+1)m:(2k+1)n}$. These are the odd spatial harmonics of $I_{m:n}$, all of which have the same intrinsic frequency $\sigma_{(2k+1)n/(2k+1)m} = \sigma_{n/m}$,

$$M_{m:n} \propto \sum_{\ell \geq 0} (2\ell + 1)^{-3} I_{(2\ell+1)m:(2\ell+1)n}.$$
(4.24)

The components $(u_h, w_h, p_h, \theta_h)$ of the modes $I_{(2\ell+1)m:(2\ell+1)n}$ have the form

$$\left.\begin{aligned}
\begin{bmatrix} u_h \\ w_h \end{bmatrix} &\propto \sigma_{n/m} \begin{bmatrix} \dfrac{n}{m} \cos(2\ell+1)m\pi x \, \sin(2\ell+1)n\pi z \\ -\sin(2\ell+1)m\pi x \, \cos(2\ell+1)n\pi z \end{bmatrix} \cos \sigma_{n/m} t, \\
\begin{bmatrix} p_h \\ \theta_h \end{bmatrix} &\propto \begin{bmatrix} \dfrac{\lambda_{n/m}}{(2\ell+1)m\pi} \sin(2\ell+1)m\pi x \, \sin(2\ell+1)n\pi z \\ \sin(2\ell+1)m\pi x \, \cos(2\ell+1)n\pi z \end{bmatrix} \sin \sigma_{n/m} t.
\end{aligned}\right\}$$
(4.25)

Figure 12 shows the vorticity and temperature deviation associated with the first few partial sums in the series expansion of $M_{5:3}$ in (4.24), as well as of $M_{5:3}$, illustrating the rapid convergence of the series (4.23) and, thus, of (4.24). It is difficult to visually distinguish the primary fields, such as the temperature deviation, of $M_{m:n}$ from those of $I_{m:n}$. The contribution of terms beyond the first term in the expansion (4.24) is more visible for the vorticity due to the larger factor, $(2k+1)^{-2}$ vs. $(2k+1)^{-3}$, resulting from the term-wise differentiation of the velocity field.

The expansion of forced responses in terms of odd harmonics of the sine wave can be obtained from the sine Fourier expansion

$$S_1(\zeta - 0.5) = -\frac{1}{4}S_2'(\zeta) = \frac{8}{\pi^2}\sum_{k\geq 0}\frac{(-1)^k}{(2k+1)^2}\sin(2k+1)\pi\zeta. \tag{4.26}$$

Expressing the linear spline as a superposition of m shifted triangular waves $S_1(\cdot - \zeta_j)$,

$$f_{n/m}(\zeta) = \sum_{j=1}^{m} a_j S_1(\zeta - \zeta_j), \tag{4.27}$$

where $\zeta_j = (2j-1)/(2m)$, $j = 1, \ldots, m$ and $a_j = \pm 0.5$ are coefficients whose signs depend on j, m and n in a non-trivial way (see Appendix E), and substituting (4.26) into (4.27) leads to

$$f_{n/m}(\zeta) = \frac{4}{\pi^2}\sum_{k\geq 0}\frac{s_k}{(2k+1)^2}\sin(2k+1)\pi\zeta, \tag{4.28}$$

with

$$s_k = 2\sum_{j=1}^{m} a_j \sin(2k+1)\pi\zeta_j, \quad k \geq 0. \tag{4.29}$$

The expression (4.29) amounts to a standard discrete sine transform of the coefficients a_j (the discrete sine transform denoted DST-IV in Britanak, Yip & Rao (2007)). The closed form expression

$$s_k = (-1)^k \sec\left(\frac{2k+1}{2}\right) r\pi, \tag{4.30}$$

with $r = n/m$, is obtained and illustrated for the case $m = 11$, $n = 4$, $k = 0$ in Appendix F. Note that s_k remains finite as long as $(2k+1)r$ is not an odd integer, i.e. r is not rational with m and n both odd. Using a density argument, the expression (4.30) extends to irrational values of r (in which case the sequence $\{s_k\}_{k\geq 0}$ never repeats), so that

$$f_r(\zeta) = \frac{4}{\pi^2}\sum_{k\geq 0}\frac{(-1)^k}{(2k+1)^2}\sec\left(\frac{2k+1}{2}\right)r\pi\sin(2k+1)\zeta\pi. \tag{4.31}$$

The waveform function is verified to be odd, $f_r(-\zeta) = -f_r(\zeta)$. The relation $(-1)^k\sin(2k+1)\zeta\pi = \cos(2k+1)(\zeta - 0.5)\pi$ emphasizes the parity of f_r around $\zeta = 0.5$. Moreover, the direct verification that f_r indeed satisfies (4.12) in the Fredholm alternative **A1** reduces to a trivial trigonometric exercise, once the right-hand side of (4.12), $2x = S_1(x - 0.5)$, is expanded for $|x| \leq 0.5$ using (4.26). While the spectral approach employed in Maas & Lam (1995) and Wotherspoon (1995), valid for any r different from resonant values $r = n/m$ with m and n odd integers, can be used to derive the infinite series expansion (4.31) directly from the functional relation (4.12), evaluating the series requires truncation to a finite number of terms and it is not clear how the truncation depends on r. On the other hand, the spatial approach leads to a linear system that provides an exact solution f_r, but only for rational $r = n/m$ with m and n of opposite parities. For irrational r, this system becomes unbounded and again a truncation, now to a finite system, must be made.

The value of (4.31) at $\zeta = 0.5$ is related to a secant zeta function introduced in Lalín, Rodrigue & Rogers (2014) that motivated the recent study in Welfert (2020), where it was shown that $f_{1/\sqrt{2}}(0.5) = 1$, as observed in figure 8.

Replacing the quantity $2x$ appearing in the components w_r, p_r and θ_r of the forced response (4.15), hereby denoted R_f, by its expression in terms of the function f_r from (4.12), and then substituting (4.31), shows that R_f can be decomposed as the superposition of responses R_{f_k},

$$R_f = \frac{4}{\pi} \sum_{k \geq 0} \frac{(-1)^k}{2k+1} R_{f_k}, \tag{4.32}$$

of the sequence of linear forced systems

$$\left.\begin{aligned} \partial_t u_k &= -\partial_x p_k + z\alpha \cos(2k+1)\pi x \sin \omega t, \\ \partial_t w_k &= -\partial_z p_k + \theta_k, \\ \partial_t \theta_k &= -w_k, \\ \partial_x u_k + \partial_z w_k &= 0. \end{aligned}\right\} \tag{4.33}$$

An explicit expression of the components $(u_k, w_k, p_k, \theta_k)$ of R_{f_k} is given in Appendix G. The pointwise convergence of (4.32) away from characteristics inside the cavity also follows directly from the Fourier cosine expansion

$$S_0(x) = \frac{4}{\pi} \sum_{k \geq 0} \frac{(-1)^k}{2k+1} \cos(2k+1)\pi x, \tag{4.34}$$

of the 2-periodic square wave S_0, whose value is $(-1)^\ell$ for $x \in (\ell - 0.5, \ell + 0.5)$, $\ell \in \mathbb{Z}$, and, in particular, 1 for $x \in (-0.5, 0.5)$. The magnitude of the velocity components and temperature deviation of R_{f_k} itself decreases inversely proportionally to k (quadratically for the pressure); see (G5). In other words, the response to (4.33) vanishes for spatially highly oscillatory forcings. As a result, (4.32) converges absolutely, whereas (4.34) does not.

Figures 13 and 14 show the partial sums of (4.32) for the vorticity η and temperature deviation θ, respectively, with an increasing number of terms, for the same $\sigma_r^2 = \omega^2$ values as those from figures 3 and 4. Note that in order to avoid $\sec(2k+1)\pi r = \infty$, the partial sums at $\sigma_r^2 = 0.1^+, 0.5^+, 0.9^-$ were computed using σ_r^2 values slightly detuned by a relative amount equivalent to ten times the machine epsilon (10×2^{-52}). Adding terms to the partial sums improves the approximation. The convergence depends on whether $\sec(2k+1)\pi r/2$ is large or not. For example, there is a big change for $\sigma_r^2 = 0.4$ when adding the fifth term and for $\sigma_r^2 = 0.6$ when adding the sixth term. This is particularly noticeable when σ_r is very close to resonances. These near resonances occur when $(2k+1)r \approx 2\ell + 1$, i.e. for every $k = m$ terms if $r \approx n/m$ with m and n both odd. For $\sigma_r^2 = 0.9^-$, $(r \approx 1/3 = n/m)$, the changes occur at terms 2 ($k = 1$, $\ell = 0$), 5 ($k = 4$, $\ell = 1$), etc.

For the most part, the comparison between the linear inviscid theory using 100 terms in the partial sums shown in figures 13 and 14 shows excellent agreement with the numerical results at the largest $R_N = 10^7$ shown in figures 3 and 4.

5. Comparison between viscous flow at large R_N and inviscid flow

This section provides quantitative comparisons between the viscous nonlinear flows obtained via direct numerical simulations (DNS) and the linear inviscid theory.
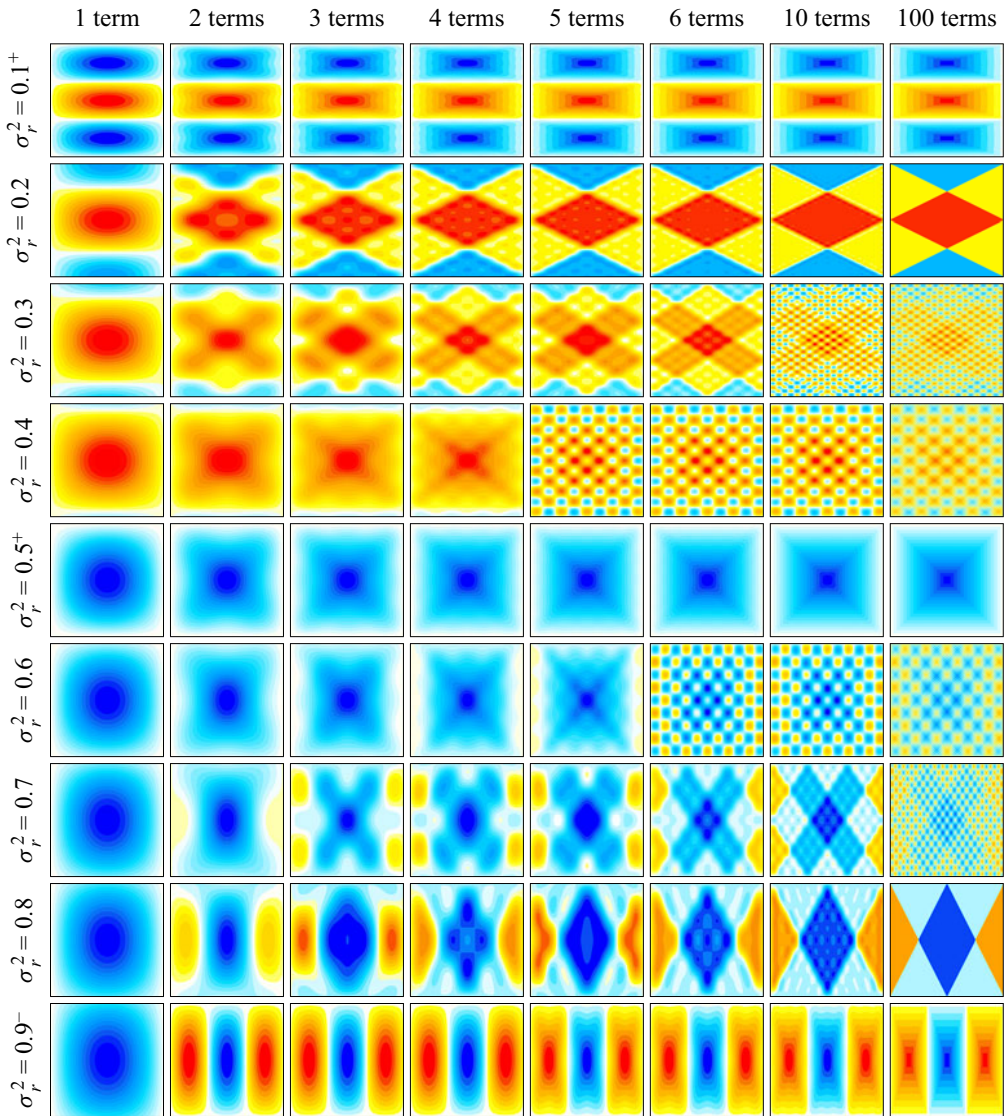
Figure 13. Plots of the vorticity η_r associated with the partial sums in the series expansion of R_f in (4.32), at σ_r^2 and a number of terms as indicated.

Global comparisons using the enstrophy and local comparisons using snapshots and horizontal profiles of the flows are made.

5.1. *Inviscid versus viscous global enstrophy and a reduced-order viscous model*

The global mean enstrophy $\langle \mathcal{E} \rangle_\tau$, defined by (3.1), of the linear inviscid responses is now compared with that of the viscous responses obtained at increasing values of R_N from figure 2(*a*). The inviscid enstrophy is given by (for details, see Appendix H)

$$\langle \mathcal{E} \rangle_\tau = \frac{\alpha^2}{r^2 \sigma_r^2} \sum_{k \geq 0} \lambda_k^{-2} \left\{ 1 + \frac{1 + r^2}{2} \left[(1 + r^2) \sec^2 \lambda_k - (3 - r^2) \frac{\tan \lambda_k}{\lambda_k} \right] \right\}. \qquad (5.1)$$
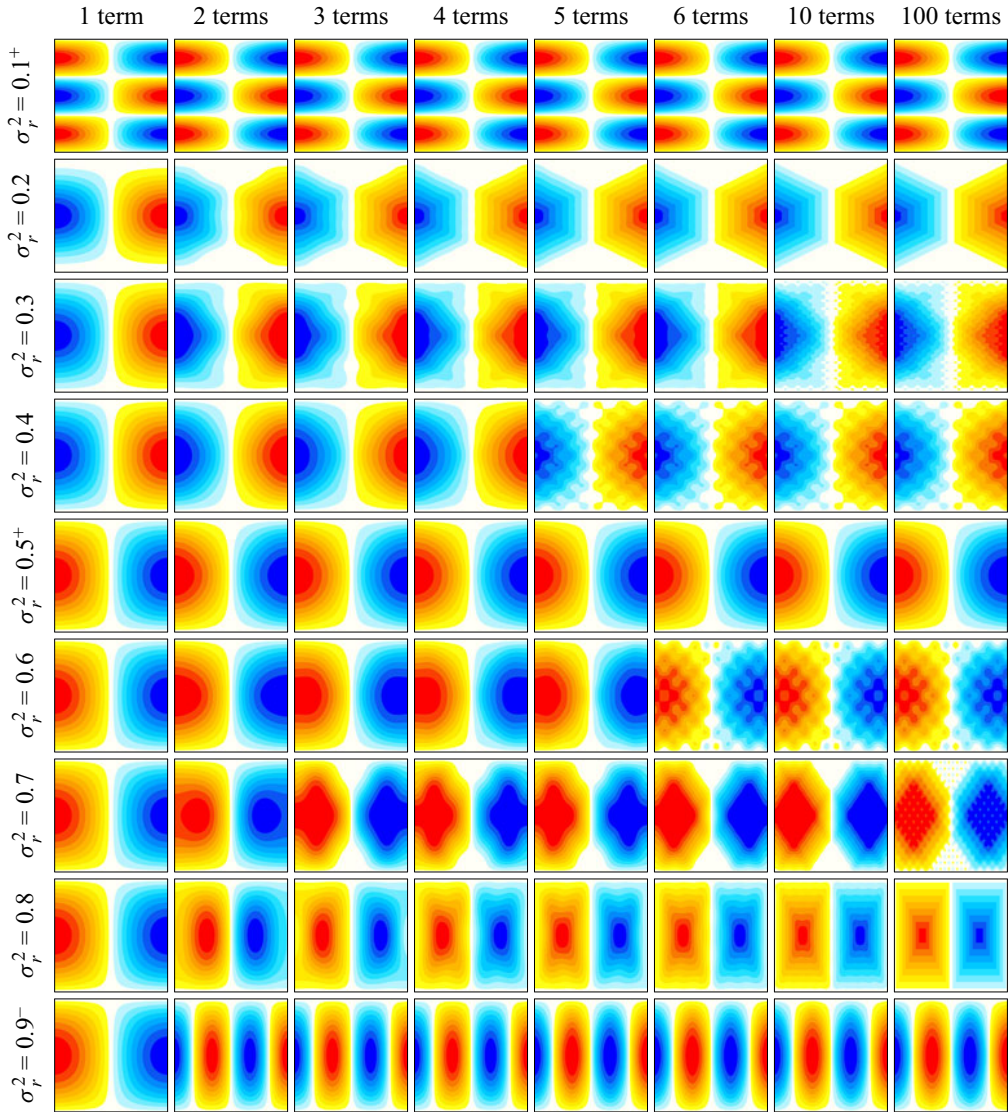
915 A85-24

Figure 14. Plots of the temperature deviation θ_r associated with the partial sums in the series expansion of R_f in (4.32), at σ_r^2 and a number of terms as indicated.

The Dirichlet series (5.1) diverges at resonances which, for the square cavity, occur for every rational $r = n/m$ with m and n both odd integers. Near a specific resonance, $\cos \lambda_k \approx 0$ for some k, (5.1) shows that the scaled global inviscid enstrophy, $(r/\alpha^2)\langle \mathcal{E} \rangle_\tau = O(r^{-3}\sigma_r^{-2}[1 + r^2]^2) = O([r + 1/r]^3)$, is invariant under the transformation $r \leftrightarrow 1/r$, i.e. $\sigma_r^2 \leftrightarrow 1 - \sigma_r^2$. Figure 15(a) illustrates this balance in the response magnitude between the $\sigma_r^2 < 0.5$ and $\sigma_r^2 > 0.5$ regimes. The graph is obtained by truncating the series (5.1) after 10 terms ($k = 9$). This truncation only retains a finite subset of rational values $r = n/m$ at which the inviscid response becomes unbounded. However, truncating the infinite series after a fixed number of terms independent of r allows for a larger set of resonances to be identified in the lower forcing frequency regime, $\sigma_r^2 < 0.5$, i.e. $r > 1$, compared with the higher frequency regime, $\sigma_r^2 > 0.5$, because of the higher frequency
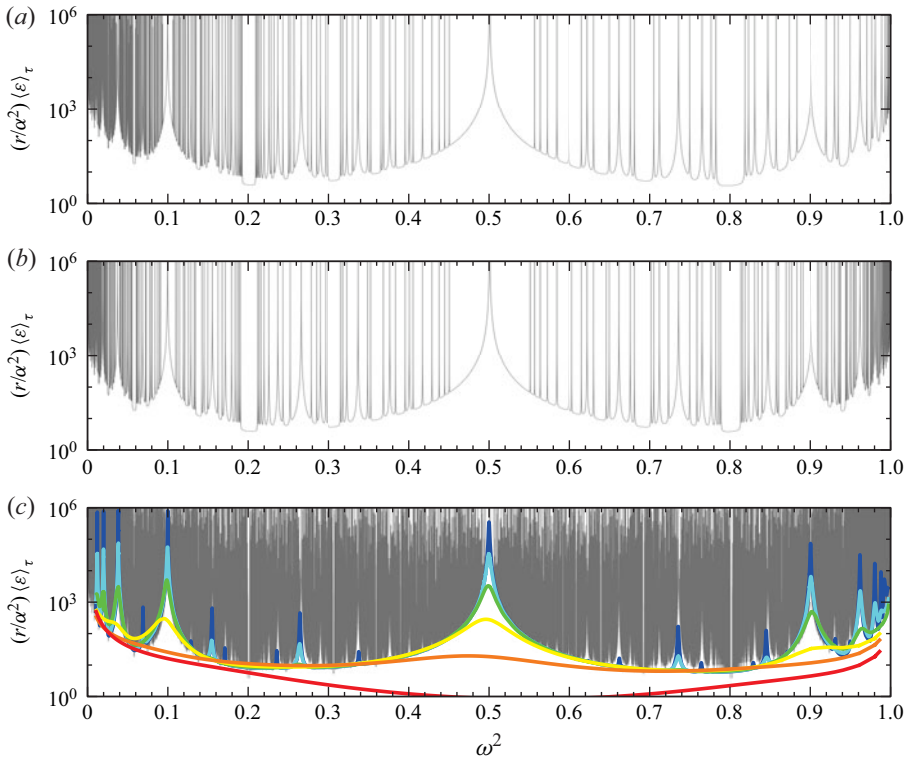
915 A85-25

Figure 15. Graph of the enstrophy $\langle \mathcal{E} \rangle_\tau$ from (5.1) scaled by α^2/r, evaluated at 10^6 values $\omega^2 \in (0, 1)$ using (a) $1 + 9 = 10$ terms, (b) $\lfloor 1 + 9/\sqrt{r} \rfloor$ term(s) or (c) $\lfloor 1 + 99/\sqrt{r} \rfloor$ term(s) in the series, where $\lfloor x \rfloor$ represents the integer part of x. Also shown in (c) are the scaled curves obtained from DNS for the different values of R_N from figure 2 using the same colours, and a viscous correction factor γ from (5.2). The supplementary movie 4 shows a frequency sweep of 9999 inviscid solutions uniformly distributed between $\omega^2 \in (0, 1)$ at phase 0 for η_r and phase $\pi/2$ for θ_r.

in the variations of $\cos \lambda_k$. In contrast, truncating after $1 + O(1/\sqrt{r})$ terms results in a comparable representation of the spatial variations of η in the x direction at $\sigma_r^2 \approx 1$ and in the z direction at $\sigma_r^2 \approx 0$, making the graph and the various resonances visually symmetric approximately $\sigma_r^2 = 0.5$; see figure 15(b). This modification in the number of terms increases the number of resonances detected by the truncated series in the $\sigma_r^2 > 0.5$ regime. For example, it decreases the frequency gap between consecutive resonances at $\sigma_r^2 \approx 0.8$, with an inverse effect in the $\sigma_r^2 < 0.5$ regime, as can be observed from the increased gap around $\sigma_r^2 \approx 0.2$. Increasing the proportionality constant of the $O(1/\sqrt{r})$ term allows for the representation of more oscillatory components throughout the σ_r^2 parameter inertial range, leading to many more resonances at $r = n/m$ with larger n and m, including those closer to $\sigma_r^2 = 0.5$ ($r = 1$), and defining an inviscid response 'envelope', shown in figure 15(c). This figure also includes the synchronous ($\sigma_r^2 = \omega^2$) response curves from DNS at various R_N from figure 2(a), adjusted for viscous effects, $\delta(r/\alpha^2)\langle \mathcal{E} \rangle_\tau$, where

$$\left. \begin{aligned} \delta &= 0.8\pi^2 R_N^{-1/2}(0.25\lambda^{1.5} + 0.75\lambda^6)^{-1}, \\ \lambda &= 4\omega^2(1 - \omega^2) = 4\sigma_r^2(1 - \sigma_r^2) = \left(\frac{2r}{1 + r^2} \right)^2. \end{aligned} \right\} \tag{5.2}$$

915 A85-26

The $O(R_N^{-1/2})$ correction leads to the asymptotic collapse (away from lower-order resonant conditions) of the response curves from figure 2(*a*) onto a single curve as R_N increases, with the proportionality constant calibrated by the response at $\omega^2 = 0.5$ ($\lambda = 1$). The factor in δ inside the parentheses is a correction away from the $r = 1$ case, in the spirit of the modal viscous reduced-order model used by Yalim *et al.* (2019*a*), to obtain an approximate critical instability curve for the linearly stratified base state subjected to purely vertical oscillatory forcing of the container. The $\lambda^{1.5}$ term controls the shape of the curves at $\omega^2 \approx 0$ or 1, while the λ^6 term controls their relative 'flatness' in the intermediate ranges around the values 0.25 and 0.75. Since $\lambda \leq 1$, this mode-dependent correction factor is larger at $\omega^2 \approx 0$ and 1, where the differences between the horizontal and vertical spatial scales of the responses are large, associated to the nearly vertical/horizontal characteristic directions, and for which the viscous boundary layers have a larger impact.

The 9999 frames in the supplementary movie 4 correspond to snapshots of η_r and θ_r at phases 0 and $\pi/2$, respectively, of the linear inviscid response flows at square forcing frequencies $\omega^2 \in (0, 1)$. The animation provides a visual catalog of the Fredholm alternative **A1** responses obtained from the truncated series (5.1) with $\lfloor 1 + 9/\sqrt{r} \rfloor$ term(s), where $\lfloor x \rfloor$ represents the integer part of x.

5.2. *Flow field comparisons*

The nonlinear viscous DNS responses from figures 3 and 4 at $R_N = 10^7$ are now compared with the inviscid responses predicted by the analysis from § 4 at similar forcing frequencies ω. These comparisons are shown in figures 16 and 17. All the inviscid responses shown were obtained using the discrete approach in physical space, described in Appendix B, rather than using the truncated spectral representations discussed in § 4.3. Responses associated with quadratic irrationals r (e.g. for $\sigma_r^2 = 0.3, 0.4, 0.6$ and 0.7) were obtained via approximations by a high-order convergent of appropriate continued fractions, similar to (4.16). Inviscid responses associated with rationals r obtained from a lower-order convergent, which correspond to slightly detuned responses, are also included for comparison with viscous results obtained at smaller R_N. For example, the case $r = 22/27$ in the vicinity of $\sigma_r^2 = 0.6$ is obtained from $r = 4/5$ using the iteration

$$\begin{bmatrix} n \\ m \end{bmatrix} \leftarrow \boldsymbol{R} \begin{bmatrix} n \\ m \end{bmatrix}, \quad \boldsymbol{R} = \begin{bmatrix} 3 & 2 \\ 3 & 3 \end{bmatrix}, \tag{5.3}$$

while the case $r = 27/22$ in the vicinity of $\sigma_r^2 = 0.4$ is obtained from $r = 5/4$ using a similar iteration based on $\boldsymbol{R}^T$ instead. Note that the ratio of coefficients of the right eigenvector of $\boldsymbol{R}$ is $r = \sqrt{2/3}$, while the same ratio for the left eigenvector is $r = \sqrt{3/2}$, values that are associated with the exact forcing frequencies.

For ease of comparison, the viscous (DNS) results at large $R_N = 10^7$ from figures 3 and 4 have been reproduced in figures 16(*a,c,e,g,i,k,m,o,q*) and 17(*a,c,e,g,i,k,m,o,q*), albeit at the fixed phases of the forcing, 0 for the vorticity η and $\pi/2$ for the temperature deviation θ. For rational $r = n/m$ with sufficiently small m and n, the DNS are very similar to the results predicted from the inviscid analysis shown in figures 16(*b,d,f,h,j,l,n,p,r*) and 17(*b,d,f,h,j,l,n,p,r*). For quadratic irrational r, such as $r = \sqrt{7/3}, \sqrt{3/2}, \sqrt{2/3}$ and $\sqrt{3/7}$, the DNS results at $R_N = 10^7$ are unable to fully capture the fractal nature of the inviscid response. For finite R_N, the viscous effects smear out the small-scale details. The DNS responses appear more like the inviscid responses obtained at nearby rational values of $r = n/m$ with moderate m and n, especially for η.
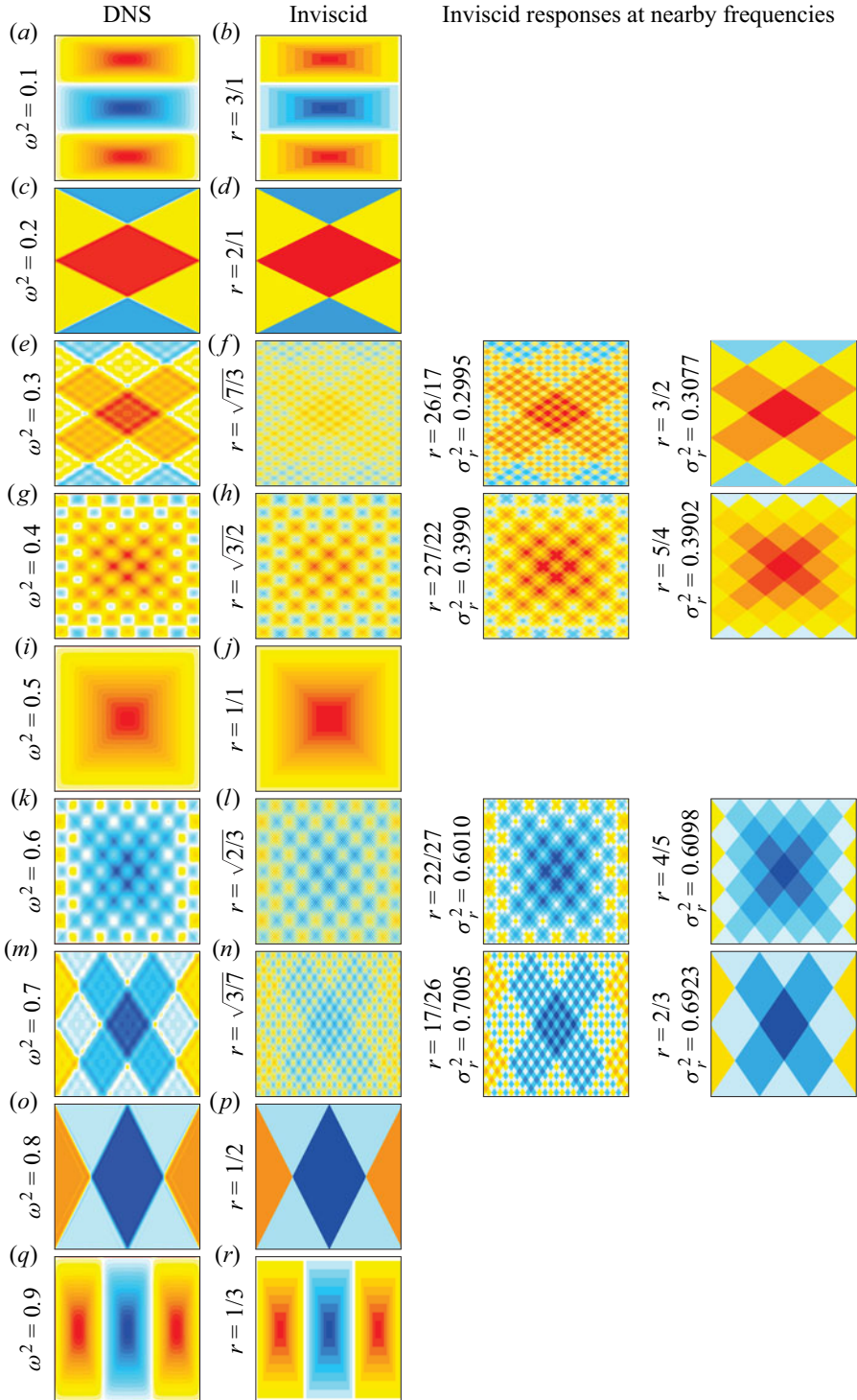
Figure 16. Vorticity η from DNS at $R_N = 10^7$ (a,c,e,g,i,k,m,o,q) and η_r from the inviscid theory (b,d,f,h,j,l,n,p,r), all at phase 0, at the indicated squared forcing frequencies ω^2 (with the corresponding r values indicated). The inviscid responses at $\sigma_r^2 = 0.3$, 0.4, 0.6 and 0.7 are fractal and are obtained as limits of sequences with rational r.
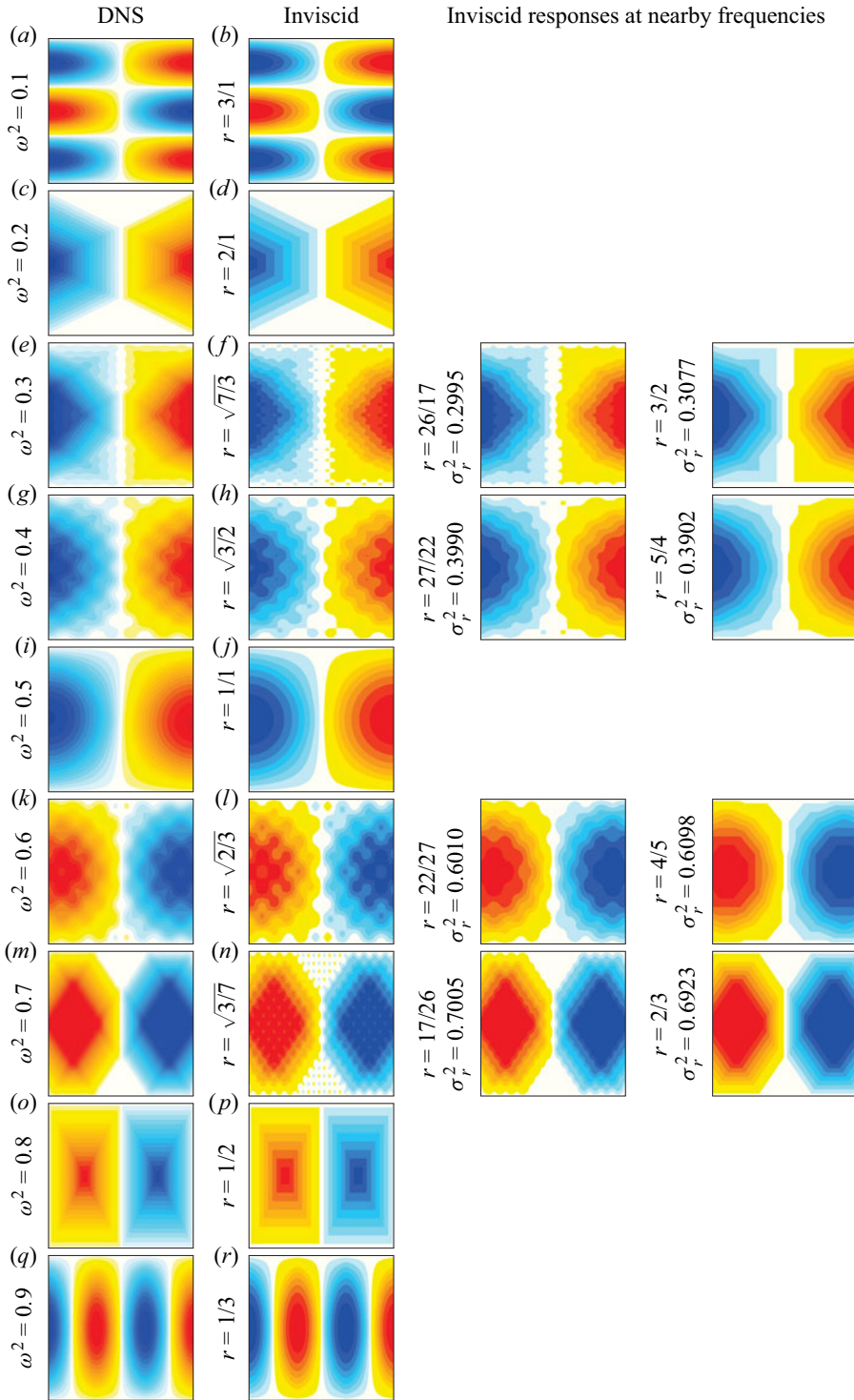
915 A85-28

Figure 17. Temperature deviation θ from DNS at $R_N = 10^7$ (a,c,e,g,i,k,m,o,q) and θ_r from the inviscid theory (b,d,f,h,j,l,n,p,r), all at phase $\pi/2$, at the indicated squared forcing frequencies ω^2 (with the corresponding r values indicated). The inviscid responses at $\sigma_r^2 = 0.3$, 0.4, 0.6 and 0.7 are fractal and are obtained as limits of sequences with rational r.

Figure 18. (*g–v*) Snapshots of η and θ from the DNS limit cycle at $R_N = 10^7$ and $\omega^2 = 0.6$ over one forcing period (see supplementary movies 1 and 2), while (*a–f,w–z,aa,ab*) show inviscid standing wave responses at maximal amplitude at r and σ_r^2 values as indicated.

Over long periods of time, even small detunings in the forcing frequency can lead to sizeable phase differences in the responses and peaks in an inviscid response at one forcing frequency that may correspond to a minimal response at a nearby forcing frequency. In the viscous DNS responses, viscous detuning at small forcing amplitudes may lead to responses that are not perfect standing waves. Figure 18 illustrates such behaviour at $\omega^2 = 0.6$ and $R_N = 10^7$. At phases 0 and π (corresponding to fractions 0 and 0.50 of a forcing period for η) or $\pi/2$ and $3\pi/2$ (i.e. fractions 0.25 and 0.75 of a forcing period for θ) the DNS response, already shown in figures 16 and 17, respectively, matches that expected from the inviscid prediction at that forcing frequency. However, at other phases, structures associated with inviscid responses at nearby σ_r^2 corresponding to $r = n/m$ with relatively small m and n appear to dominate. In particular, the structure associated with the resonant response at $r = 9/11$ becomes clearly visible at phases where a standing wave response would be expected to vanish. Which inviscid response is identified in the DNS at a particular phase depends on the relative energies of the various responses at nearby (i.e. viscously detuned) forcing frequencies in relation to viscous effects as measured by R_N.

5.3. *Horizontal profile comparisons*

This subsection compares the horizontal profiles at $z = 0$ of the vorticity η and temperature deviation θ from the DNS at $R_N = 10^7$ with the linear inviscid theory. The comparison is performed at the maximal phase for the respective fields. In order to do this, the corresponding inviscid η_r and θ_r need to be evaluated from the waveform function f_r. How these are evaluated depends on whether the response is forced or resonant.

For the forced responses, (4.15) results in

$$\alpha^{-1} \begin{bmatrix} \eta_r \\ \theta_r \end{bmatrix} = (1 - \sigma_r^2)^{-1} \begin{bmatrix} \sigma_r^{-1}(f_r'(x) - \sigma_r^2) \\ f_r(x) - x \end{bmatrix}, \qquad (5.4)$$

with η_r affinely related to the derivative of θ_r. For the resonant responses, (4.22) leads to

$$\begin{bmatrix} \eta_r \\ \theta_r \end{bmatrix} \propto 2 \begin{bmatrix} \sigma_r^{-1} f_r'(x) \\ f_r(x) \end{bmatrix}, \qquad (5.5)$$

with η_r now directly proportional to the derivative of θ_r.

915 A85-30

The profiles from the DNS and linear inviscid theory are shown in figure 19. The resonant responses are in figures 19(*a*,*b*) and 19(*i*,*j*) and the forced responses in figures 19(*c*,*d*) through 19(*g*,*h*). For $\omega^2 = \sigma_r^2 = 0.5$ with $r = 1/1$, the response is resonant and $f_r(x) = 4x(1 - |x|)$ for $|x| \leq 0.5$ from (4.20). This waveform function f_r is piecewise quadratic. Likewise, for $\omega^2 = \sigma_r^2 = 0.9$ with $r = 1/3$, the response is resonant and (4.21) yields the piecewise quadratic $f_r(x) = 4(3x)(1 - 3|x|)$ for $|x| \leq 1/6$, and is extended by symmetry and periodicity for $|x| > 1/6$. For the forced response at $\omega^2 = \sigma_r^2 = 0.8$ with rational $r = 1/2$, $f_r(x) = |x + 0.25| - |x - 0.25|$ for $|x| \leq 0.5$. This piecewise linear f_r is obtained either by evaluating the spectral series (4.31) for $f_{1/2}$ in closed form, or by solving the system (4.14) and collecting the linear pieces.

For the forced responses at $\omega^2 = \sigma_r^2 = 0.6$ and 0.7, for which r is irrational, the evaluation of f_r is no longer straightforward. The inviscid profiles that are illustrated in figures 19(*c*,*d*) and 19(*e*,*f*) were obtained by truncating the series representation of f_r, equation (4.31), as indicated in the figure. The number of terms retained is determined such that the resulting fields capture the oscillatory behaviour of the DNS responses without introducing high spatial frequency content due to large coefficients $\sec[(2k + 1)/2]\pi r$ for arbitrarily large k when r is irrational. While the truncation captures the oscillations in the DNS, it overestimates their amplitude. This is partly due to the inviscid theory not having viscous damping.

In order to improve the comparison, filtering techniques, such as the use of mollifiers (Tadmor 2007), may be applied to the series representation of f_r. The use of a mollifier softens the effects of the truncation and provides a much better quantitative account of the viscous results in the DNS. This is illustrated in figure 20, where the mollifier $\exp(-[(2k + 1)\pi/40]^2)$ is used for $\omega^2 = \sigma_r^2 = 0.6$ and the mollifier $\exp(-[(2k + 1)\pi/70]^4)$ is used for $\omega^2 = \sigma_r^2 = 0.7$. The factors 40 and 70 are fitting parameters, on the order of $R_N^{1/4} \approx 56$. These factors are consistent with the $R_N^{-1/2}$ factor appearing in the viscous dissipation correction (5.2) at the global enstrophy level. The power 2 in the first mollifier corresponds to the Gaussian filtering associated with Laplacian dissipation. The power 4 in the second mollifier corresponds to a biharmonic filtering, known for its scale selectivity. It is used extensively in ocean models (Griffies 2004), and its tendency to overshoot large changes in the data (Delhez & Deleersnijder 2007) is a feature exploited here to better capture the DNS results.

6. Summary, discussion and perspectives

6.1. *Summary*

A static vertically stratified fluid, with temperature $T = z$, in a rectangular container is viscously stable. In order to have a sustained non-trivial response flow, the system needs to be continuously forced. The nature of the response flow depends on the nature of the forcing. Here, we consider the effects of subjecting the container to small horizontal oscillations that are harmonic in time, leading to a horizontally modulated effective gravity. The static stratified state is not an equilibrium of the forced system, and the response flow is non-trivial for all non-zero forcing frequencies ω and amplitudes α. The flows obtained via DNS of the Navier–Stokes–Boussinesq equations are synchronous with the forcing and retain the spatio-temporal symmetries of the forced system. As viscous effects are reduced (by increasing R_N, the buoyancy frequency relative to the viscous time scale), these flows tend to be standing waves with spatial structure that is increasingly less regular, with nearly piecewise constant or piecewise linear vorticity distributions, depending on the forcing frequency.
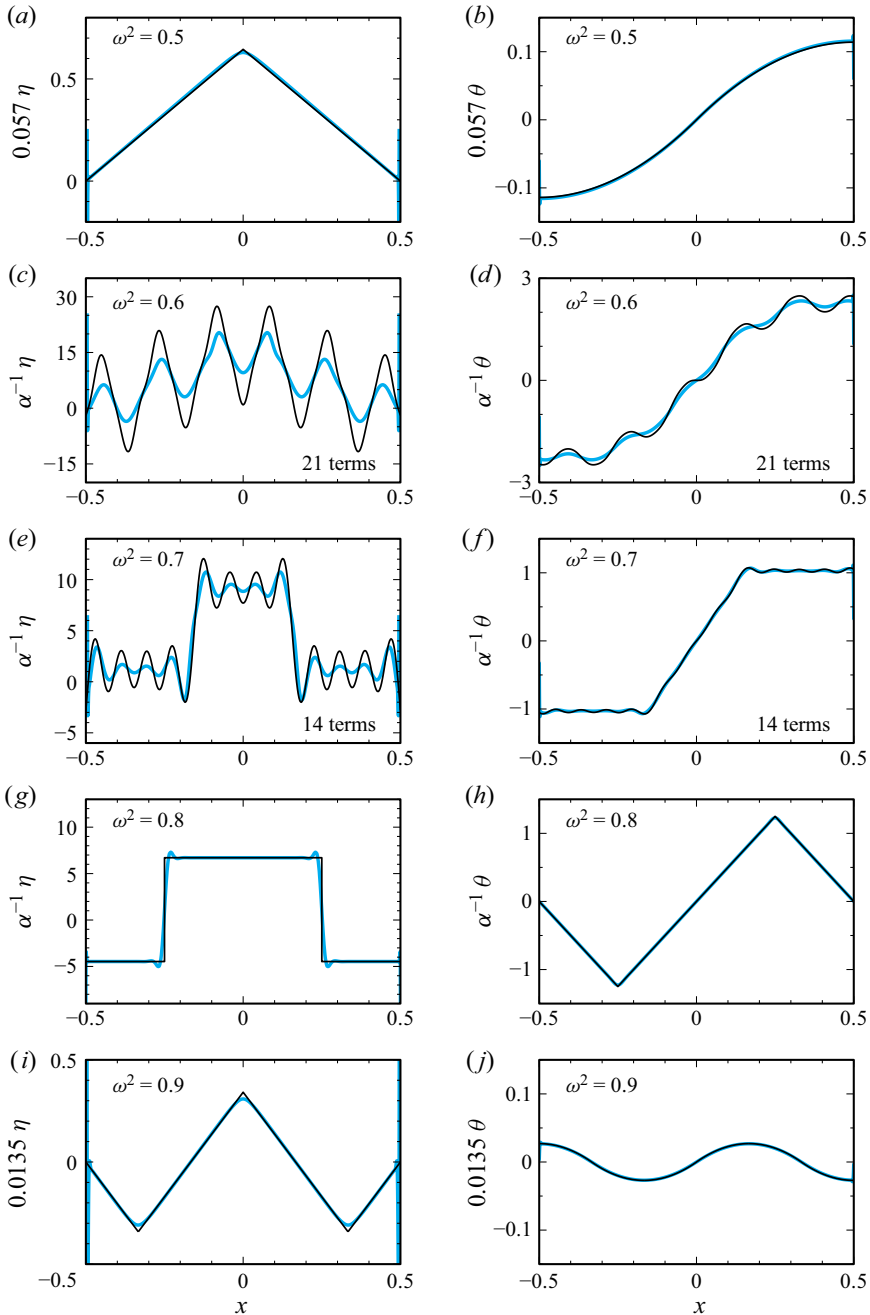
Figure 19. Horizontal profiles of the (scaled) vorticity η and temperature deviation θ at $z = 0$ and ω^2 as indicated. The black profiles correspond to the inviscid prediction based on the expression (4.22) (for a,b,i,j) or (4.15) (for c–h). The waveform function f_r used in these expressions is obtained either explicitly for the cases $\omega^2 = 0.5$, 0.8 and 0.9 associated with rational values of r, or via the series (4.31) truncated to the indicated number of terms for the cases $\omega^2 = 0.6$ and 0.7 associated with irrational values of r. An appropriate factor is used to scale the resonant cases (eigenmodes; a,b,i,j) in order to facilitate the comparison with the DNS response obtained at $R_N = 10^7$ from figure 5 (here shown in cyan).
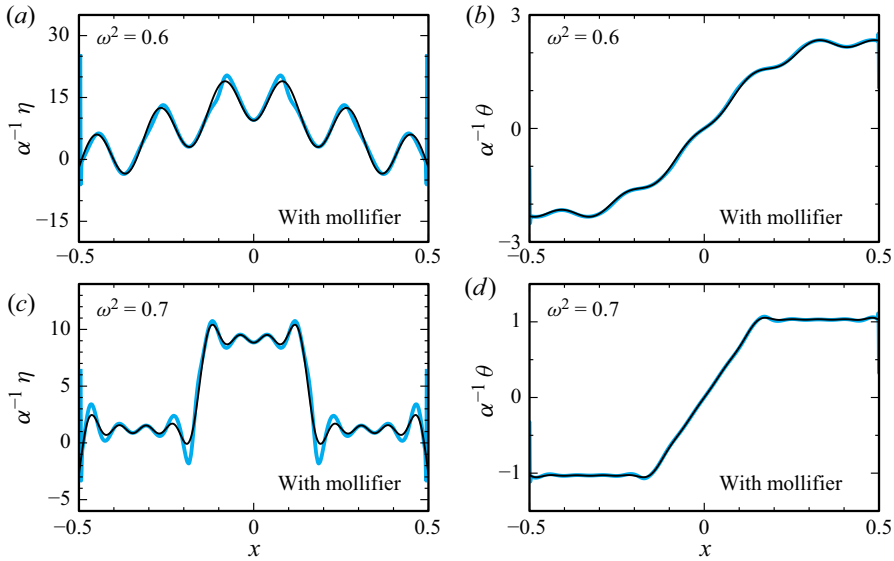
Figure 20. Horizontal profiles of the (scaled) vorticity η and temperature deviation θ at $z = 0$ similar to figures 19(c,d) and 19(e,f), but using a mollifier rather than hard truncation of the spectral series (4.31) of the waveform function f_r to account for viscous effects.

The high R_N flows are well described in the inviscid limit by a perturbation analysis of the unforced equilibrium using the forcing amplitude as the small perturbation parameter. The forcing term in the full nonlinear problem, $\alpha T \sin \omega t$, reduces to $\alpha z \sin \omega t$ in the first-order perturbed system, which is linear and non-homogeneous with Dirichlet boundary conditions. This non-homogenous linear boundary value problem is reduced to a Poincaré equation for the temperature deviation, which is independent of the forcing.

The Poincaré equation is solved by a general standing wave ansatz for the temperature deviation, motivated by the DNS results. Substituting this into the first-order perturbation system leads to corresponding velocity components and pressure. Enforcing symmetries and boundary conditions on these then leads to a system of functional equations for the waveform function f, one of which depends on the forcing. The solutions depend on whether the forcing resonates or not with the intrinsic modes of the static vertically stratified fluid in the container, as categorized by a Fredholm alternative for f. Forced responses are obtained at forcing frequency ω such that $\omega^2 = 1/(1 + r^2)$, with r being irrational, or $r = n/m$ being rational with integers m and n of opposite parities. The linear inviscid system has then a unique response flow (alternative **A1**) which scales with the forcing amplitude α. For rational $r = n/m$ with m and n of opposite parities, a linear spline f can be determined by solving a non-homogeneous linear system. The resulting response has piecewise constant vorticity which is discontinuous across characteristic lines and forms a regular harlequin pattern. For irrational r, the waveform function f is better expressed in the form of a spectral Dirichlet series. At least for quadratic irrationals r, the sequence of rational cumulants of the continued fraction representation of r leads to self-similar properties of f and the harlequin pattern of the vorticity becomes fractal.

Resonant responses are obtained at forcing frequencies $\omega^2 = 1/(1 + r^2)$ for $r = n/m$ with integers m and n both odd (alternative **A2**). These responses correspond to solutions of the unforced, homogeneous inviscid linear perturbation equations and are intrinsic eigenmodes of the unforced system. The spatial structure of the specific modes excited by the particular forcing is obtained by considering the limit of forced responses as the forcing

915 A85-33

frequency approaches a resonant frequency. The response flow becomes unbounded, with piecewise quadratic velocity and temperature deviation, and, thus, a piecewise linear vorticity field, and can be represented as a superposition of an infinite set of odd spatial harmonics of smooth intrinsic modes of the unforced system.

Models of viscous dissipation both at the global enstrophy level and at the local level in a horizontal cut via mollifiers were introduced in the inviscid model to account for viscous effects at finite R_N. The use of filtering strategies in post-processing is in general necessary when differentiating low regularity solutions.

6.2. *Discussion*

The linear inviscid theory provides an increasingly more accurate description of the DNS responses as R_N is increased, highlighting the tendency of these DNS response flows to become less regular, and even fractal-like for certain forcing frequencies, as viscous regularization is reduced. These non-smooth flow features originate in the existence of non-smooth solutions of the Poincaré equation, a possibility already raised by Aldridge (1975). Low regularity solutions were obtained in Maas & Lam (1995) by solving the Poincaré equation in a geometry with at least one wall oblique to the direction of stratification or the direction perpendicular to the stratification, with homogeneous (Dirichlet) boundary conditions specified at the boundaries. In the present study the square cavity considered has all walls either parallel or orthogonal to gravity and the low regularity of the solutions is a consequence of the oscillatory horizontal forcing being orthogonal to the direction of gravity.

Solutions with low regularity that have been observed in stratified as well as rotating flows are more typically beams with a concentrated delta-like distribution of vorticity along rays (in two dimensions) or vortex sheets (in three dimensions). These beams usually originate from localized forcings and are aligned with the characteristics, typically forming a St Andrew's cross pattern (Görtler 1943; Mowbray & Rarity 1967; Voisin 2003). The piecewise constant vorticity solutions obtained here constitute a more regular class of beams, with energy distributed over the container rather than focused in rays or sheets, and can be overshadowed by these stronger beams when the latter are present, as happens, for example, in numerical simulations of parametrically forced rotating flows (Wu *et al.* 2020).

The present study has focused on the very small forcing amplitude regime. The question of what happens as this amplitude is increased remains open, and of current interest (e.g. Savaro *et al.* 2020). The transition to internal wave turbulence is expected to occur at smaller forcing amplitudes as R_N is increased as a result of higher-order resonances becoming less viscously damped (Aldridge & Toomre 1969). We are currently investigating how the response flows lose stability as the forcing amplitude is increased.

When $r = n/m$, with integers m and n of opposite parities, the linear inviscid system (4.1) admits, under alternative **A1**, a unique synchronous forced response that scales with the forcing amplitude. However, (4.1) also admits solutions which are not standing waves for such values of r, for example, a superharmonic component evolving at twice the forcing frequency, 2ω, if $4\omega^2 < 1$. The spatio-temporal symmetries then allow for superharmonic resonant responses under alternative **A2**. Such a resonance is triggered by second-order nonlinear contributions, but it is moderated by viscous effects. For large values of R_N (larger than those considered in the present study for the very low forcing amplitude α used), it is expected that viscous damping is sufficiently reduced so that the superharmonic resonant response will dominate.

6.3. *Extensions and further remarks*

In the present study we have considered the square cavity. However, the results are straightforwardly extended to rectangular cavities of width-to-depth aspect ratio Γ. The dispersion relation (4.5) then becomes $\sigma_r^2 = \Gamma^2/(\Gamma^2 + r^2)$, with responses according to Fredholm alternatives **A1** and **A2** depending on r in a similar fashion as when $\Gamma = 1$. If the container is not rectangular, for example, due to walls at oblique angles to gravity, or is tilted, the responses may become non-trivial as a result of the peculiar reflections of internal waves, which may lead to internal wave attractors or focusing into edges or corners. While some aspects of this has been previously studied (e.g. Maas & Lam 1995; Wotherspoon 1995), there is still much to learn (e.g. Bajars *et al.* 2013; Pillet *et al.* 2018; Pillet, Maas & Dauxois 2019), and approaches from the study of how inertial waves reflect in the obliquely rotating cube (Wu *et al.* 2020) can be adapted for the internal wave problem.

In order to determine whether the low regularity patterns in the 2-D solutions persist in a 3-D container, two cases, corresponding to $\omega^2 = 0.2$ and $\omega^2 = 0.5$, were simulated at $R_N = 10^6$ and $\alpha = 1.75 \times 10^{-6}$ in a box $[-0.5, 0.5] \times [-0.2, 0.2] \times [-0.5, 0.5]$ with no-slip, insulated walls at $y = \pm 0.2$. The spanwise aspect ratio 0.4 is the same as that used in the experiments of Benielli & Sommeria (1998) and the simulations of Yalim *et al.* (2020) for the vertically forced system. The $\omega^2 = 0.2$ case is a prototypical example of a forced response in the 2-D setting (Fredholm alternative **A1**), and the $\omega^2 = 0.5$ case corresponds to a resonant response associated with the main peak in the Bode diagram (figure 2) in the 2-D setting (Fredholm alternative **A2**). Figure 21(*a–d*) shows the 2-D DNS solutions from figures 3 and 4 for comparison with the figure 21(*e–h*) showing the vorticity and temperature deviation at the spanwise midplane $y = 0$ of the 3-D DNS solutions. For $\omega^2 = 0.2$, the solutions are qualitatively the same and quantitatively the 3-D vorticity level is approximately 77 % that of the 2-D vorticity, while the 3-D temperature deviation is approximately 2 % larger. For $\omega^2 = 0.5$, the solutions are also qualitatively the same, but the 3-D vorticity and temperature deviation levels are both approximately 46 % those of the corresponding 2-D solution. From the 2-D study, it appears that resonant responses tend to be more affected by viscous effects than the forced responses are. The viscous dissipation in the boundary layers along the spanwise walls of the 3-D container are also responsible for dampening the response. This warrants a more detailed separate investigation. As noted by Benielli & Sommeria (1998), the effects of friction in parametrically forced stratified confined flows are not well understood, and, hence, neither are those associated with variations of the Prandtl number.

Author ORCIDs.
- Hezekiah Grayer II https://orcid.org/0000-0002-8103-8451;
- Jason Yalim https://orcid.org/0000-0001-6866-9833;
- Bruno D. Welfert https://orcid.org/0000-0002-9134-2078;
- Juan M. Lopez https://orcid.org/0000-0002-4580-6505.
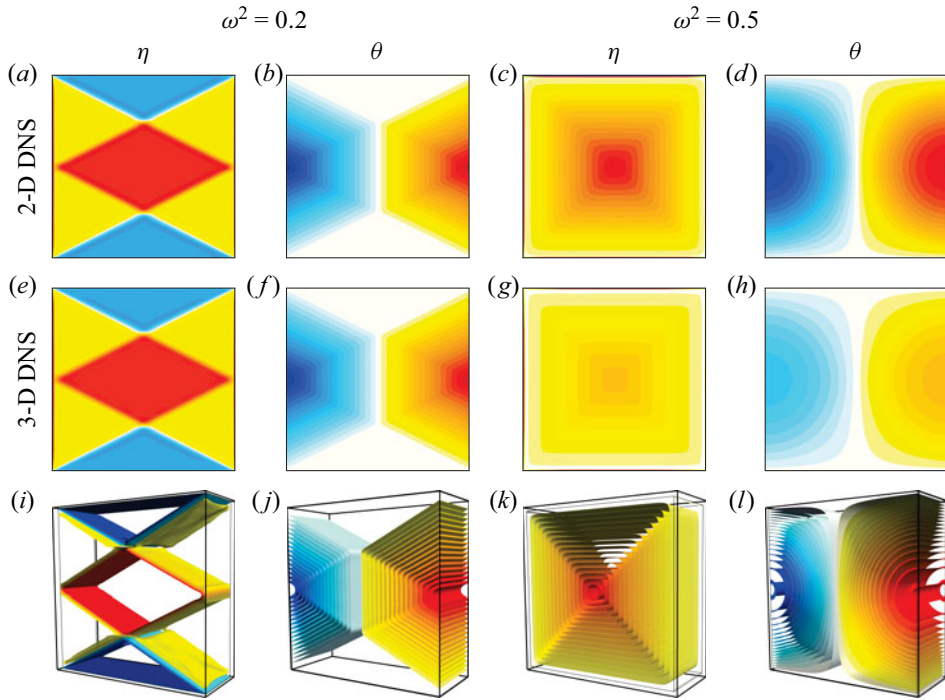
Figure 21. Panels (*a–d*) show the 2-D η and θ at $R_N = 10^6$ and ω^2 as indicated (repeated from figures 3 and 4 for ease of comparison) and panels (*e–g*) show the 3-D η and θ in the spanwise midplane using the same colour levels as in the 2-D cases (*a–d*). Panels (*i–l*) show the corresponding isosurfaces of the 3-D solutions (using a different colour map), with the boundary layer regions clipped.

Appendix A. The relation between $f_{1/r}$ and f_r and the corresponding flow responses

If f_r is odd and obeys (4.10) and (4.12), then the function $f_{1/r}$ defined by

$$f_{1/r}(\zeta) = \zeta - \frac{1}{r} f_r(r\zeta), \quad |\zeta| \leq \frac{1+r}{2r}, \tag{A1}$$

is also odd and obeys (4.10) and (4.12). To see this, assume that $f_r : [-(1+r)/2, (1+r)/2] \to \mathbb{R}$ is odd and obeys the conditions

$$f_r(\xi + 0.5) + f_r(\xi - 0.5) = 2\gamma\xi, \quad |\xi| \leq r/2, \tag{A2}$$

$$f_r(x + r/2) + f_r(x - r/2) = 2(1 - \gamma)x, \quad |x| \leq 0.5, \tag{A3}$$

where $\gamma \in \mathbb{R}$. We show that the function $f_{1/r}$, defined by (A1), obeys similar properties in appropriate ranges of its argument. For $|\xi| \leq 1/(2r)$, we obtain

$$
\begin{aligned}
f_{1/r}(\xi + 0.5) + f_{1/r}(\xi - 0.5) &= 2\xi - [f_r(x + r/2) + f_r(x - r/2)]/r \\
&= 2\xi - 2(1 - \gamma)x/r = 2\gamma\xi,
\end{aligned}
\tag{A4}
$$

here $x = r\xi$ with $|x| \leq 0.5$. On the other hand,

$$
\begin{aligned}
f_{1/r}(x + 0.5) + f_{1/r}(x - 0.5) &= 2x - [f_r(\xi + 0.5) + f_r(\xi - 0.5)]/r \\
&= 2x - 2\gamma\xi/r = 2(1 - \gamma)x
\end{aligned}
\tag{A5}
$$

for $\xi = rx$ with $|\xi| \leq r/2$ and $|x| \leq 0.5$. For $\gamma = 0$, (A2) and (A3) are then equivalent to (4.10) and (4.12), respectively.

The relation (A1) is involutory, $f_{1/(1/r)} = f_r$ on the interval $[-(1 + r)/2, (1 + r)/2]$, and this provides a direct connection between the corresponding velocities of the forced responses at r (with frequency σ_r) and at $1/r$ (with frequency $\sigma_{1/r} = \sqrt{|1/2 - \sigma_r^2|}$), namely

$$\begin{bmatrix} u_{1/r}(z, x, t) \\ w_{1/r}(z, x, t) \end{bmatrix} = \frac{r\cos(r\sigma_r t)}{\cos(\sigma_r t)} \begin{bmatrix} w_r(x, z, t) \\ u_r(x, z, t) \end{bmatrix}. \tag{A6}$$

The relations between $(p_{1/r}, \theta_{1/r})$ and (p_r, θ_r) are not as straightforward. In particular, $\theta_{1/r}$ cannot be simply related to θ_r, and $p_{1/r}$ is only related to p_r up to a quadratic pressure term proportional to α. Nevertheless, the identity (A1) shows that the response (4.15) associated with $1/r > 1$ can be reconstructed from that obtained for $r < 1$. In particular, (A6) shows that the velocity oscillation amplitude associated with $1/r$ is r times that of the velocity oscillation amplitude associated with r. For $0 < r < 1$, the vorticity response at forcing frequency $\omega^2 = \sigma_{1/r}^2 < 1/2$ oscillates at lower amplitude and angular frequency, $\eta_{1/r}(z, x, t) \sim -r\eta_r(x, z, t)$ and $r\sigma_r$, than the vorticity response $\eta_r(x, z, t)$ at $\omega^2 = \sigma_r^2 > 1/2$. This accounts for the tendency in the $\langle \mathcal{E} \rangle_\tau$ vs. ω^2 response curves shown in figure 2(a) to slightly increase (on a logarithmic scale) in proportion to $1/r = \sqrt{(1 - \omega^2)/\omega^2}$, rather than $1/r^2$. This is more markedly visible at small ω.

The relation (A1) can be used to determine $f_r(\zeta) = \zeta - rf_{1/r}(\zeta/r)$ from $f_{1/r}$ for $r > 1$, i.e. $\omega^2 < 0.5$. The knots ζ of f_r are related to the knots $x = \zeta/r$ of $f_{1/r}$ by $\zeta = rx$, and the corresponding value of f_r becomes $f_r(\zeta) = rx - rf_{1/r}(x)$. The relations

$$\sigma_{1/r} = r\sigma_r \quad \text{and} \quad c_{1/r} = r^2 c_r \tag{A7a,b}$$

then show that

$$\begin{aligned}
\frac{1}{\cos r\sigma_r t} \begin{bmatrix} u_{1/r}(z, x, t) \\ w_{1/r}(z, x, t) \end{bmatrix} &= c_{1/r}\sigma_{1/r} \begin{bmatrix} [f_{1/r}(z + x/r) - f_{1/r}(z - x/r)]/r \\ 2z - f_{1/r}(z + x/r) - f_{1/r}(z - x/r) \end{bmatrix} \\
&= r^2 c_r \sigma_r \begin{bmatrix} 2 - f_r(x + rz) + f_r(x - rz) \\ f_r(x + rz) - f_r(x - rz) \end{bmatrix} \\
&= \frac{r}{\cos \sigma_r t} \begin{bmatrix} w_r(x, z, t) \\ u_r(x, z, t) \end{bmatrix}.
\end{aligned} \tag{A8}$$

A direct consequence of (A8) is the relation between the corresponding vorticities,

$$\eta_{1/r}(z, x, t) = -\frac{r\cos r\sigma_r t}{\cos \sigma_r t}\eta_r(x, y, t). \tag{A9}$$

Appendix B. The linear system (4.14) and its solution

We illustrate the construction and solution of the linear system (4.14) obtained by enforcing the condition (4.12) arising from the Fredholm alternative **A1** in the rational case $r = n/m$ with $m = 11$ and $n = 4$.

Let $x_j = j/(2m) = j/22$ and $f_j = f(x_j)$ for $j \in \mathbb{Z}$. Evaluating (4.12) at $x_j, j = 1, \ldots, 11$, yields the system

$$
\begin{bmatrix}
1 & & & & 1 & & & & & \\
& 1 & & & & 1 & & & & \\
& & 1 & & & & 1 & & & \\
& & & 1 & & & & 1 & & \\
& & & & 1 & & & & 1 & \\
& & & & & 1 & & & & 1 \\
& & & & & & 1 & & & & 1 \\
& & & & & & & 1 & & & 1 \\
& & & & & & & & 1 & & 1 \\
& & & & & & & & & 1 & 1 \\
& & & & & & & & & & 1
\end{bmatrix}
\begin{bmatrix}
f_{-3} \\ f_{-2} \\ f_{-1} \\ f_0 \\ \hline f_1 \\ f_2 \\ f_3 \\ f_4 \\ f_5 \\ f_6 \\ f_7 \\ f_8 \\ f_9 \\ f_{10} \\ f_{11} \\ \hline f_{12} \\ f_{13} \\ f_{14} \\ f_{15}
\end{bmatrix}
= 2
\begin{bmatrix}
x_1 \\ x_2 \\ x_3 \\ x_4 \\ x_5 \\ x_6 \\ x_7 \\ x_8 \\ x_9 \\ x_{10} \\ x_{11}
\end{bmatrix}. \qquad (B1)
$$

The parity conditions $f_{-j} = -f_j, j = 0, 1, 2, 3$ (in particular, $f_0 = 0$) and symmetries $f_{11+j} = f_{11-j}, j = 1, 2, 3, 4$, reduce (B1) to the $m \times m = 11 \times 11$ system (4.14),

$$
\mathbf{A}f(x) =
\begin{bmatrix}
-1 & 1 & & & & & & & & & \\
-1 & & 1 & & & & & & & & \\
-1 & & & 1 & & & & & & & \\
& & & & 1 & & & & & & \\
1 & & & & & 1 & & & & & \\
& 1 & & & & & 1 & & & & \\
& & 1 & & & & & 1 & & & \\
& & & 1 & & & & & 1 & & \\
& & & & 1 & & & & & 1 & \\
& & & & & 1 & 1 & & & & \\
& & & & & & 2 & & & &
\end{bmatrix}
\begin{bmatrix}
f_1 \\ f_2 \\ f_3 \\ f_4 \\ f_5 \\ f_6 \\ f_7 \\ f_8 \\ f_9 \\ f_{10} \\ f_{11}
\end{bmatrix}
= 2
\begin{bmatrix}
x_1 \\ x_2 \\ x_3 \\ x_4 \\ x_5 \\ x_6 \\ x_7 \\ x_8 \\ x_9 \\ x_{10} \\ x_{11}
\end{bmatrix}
= 2x, \qquad (B2)
$$

obtained by mirroring columns of the matrix in (B1) around the greyed-out columns. The system (B2) can be split into two independent subsystems for odd- and even-indexed values (a consequence of m and n having opposite parities),

$$
\begin{bmatrix}
-1 & 1 & & & \\
-1 & & 1 & & \\
1 & & & 1 & \\
& 1 & & & 1 \\
& & 1 & 1 & \\
& & & 2 &
\end{bmatrix}
\begin{bmatrix}
f_1 \\ f_3 \\ f_5 \\ f_7 \\ f_9 \\ f_{11}
\end{bmatrix}
= 2
\begin{bmatrix}
x_1 \\ x_3 \\ x_5 \\ x_7 \\ x_9 \\ x_{11}
\end{bmatrix},
\qquad
\begin{bmatrix}
-1 & 1 & & \\
& & 1 & \\
1 & & & 1 \\
& 1 & & 1 \\
& & 1 & 1
\end{bmatrix}
\begin{bmatrix}
f_2 \\ f_4 \\ f_6 \\ f_8 \\ f_{10}
\end{bmatrix}
= 2
\begin{bmatrix}
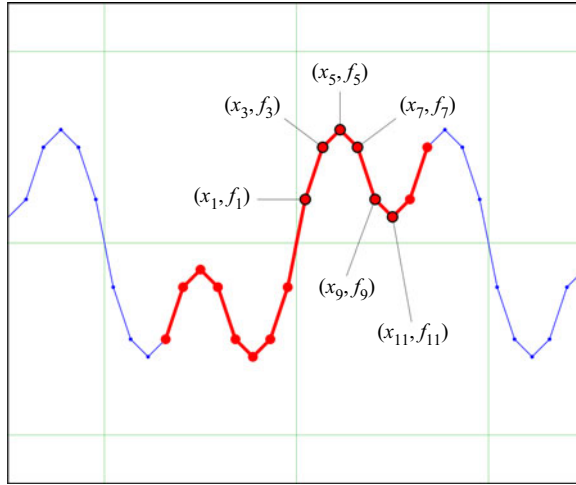x_2 \\ x_4 \\ x_6 \\ x_8 \\ x_{10}
\end{bmatrix}.
$$
$$(B3a,b)$$

Figure 22. The 2-periodic linear spline $f_{4/11}$. The dots indicate the interpolating points. All data can be obtained from (x_j, f_j), $j = 1, 3, 5, 7, 9$ and 11, via the symmetries approximately $x = 0$ and $x = 0.5$. The range of x-values associated with the red part is the range $[-(1 + 4/11)/2, (1 + 4/11)/2] \approx [-0.68, 0.68]$ where f must be defined in order to evaluate the response everywhere in the square cavity.

The two subsystems can in turn be permuted into lower triangular bidiagonal systems,

$$
\begin{bmatrix} 2 \\ 1 & -1 \\ & 1 & 1 \\ & & 1 & 1 \\ & & & 1 & -1 \\ & & & & 1 & 1 \end{bmatrix} \begin{bmatrix} f_7 \\ f_1 \\ f_9 \\ f_5 \\ f_3 \\ f_{11} \end{bmatrix} = 2 \begin{bmatrix} x_{11} \\ x_3 \\ x_5 \\ x_9 \\ x_1 \\ x_7 \end{bmatrix}, \quad \begin{bmatrix} 1 \\ 1 & 1 \\ & 1 & -1 \\ & & 1 & 1 \\ & & & 1 & 1 \end{bmatrix} \begin{bmatrix} f_8 \\ f_6 \\ f_2 \\ f_{10} \\ f_4 \end{bmatrix} = 2 \begin{bmatrix} x_4 \\ x_{10} \\ x_2 \\ x_6 \\ x_8 \end{bmatrix}, \quad \text{(B4a,b)}
$$

with (re-ordered) solutions

$$
\begin{bmatrix} f_1 \\ f_3 \\ f_5 \\ f_7 \\ f_9 \\ f_{11} \end{bmatrix} = \frac{1}{22} \begin{bmatrix} 5 \\ 11 \\ 13 \\ 11 \\ 5 \\ 3 \end{bmatrix}, \quad \begin{bmatrix} f_2 \\ f_4 \\ f_6 \\ f_8 \\ f_{10} \end{bmatrix} = \frac{1}{22} \begin{bmatrix} 8 \\ 12 \\ 12 \\ 8 \\ 4 \end{bmatrix} = \frac{1}{2} \begin{bmatrix} 1 & 1 \\ & 1 & 1 \\ & & 1 & 1 \\ & & & 1 & 1 \\ & & & & 1 & 1 \end{bmatrix} \begin{bmatrix} f_1 \\ f_3 \\ f_5 \\ f_7 \\ f_9 \\ f_{11} \end{bmatrix}. \quad \text{(B5a,b)}
$$

The connection between odd- and even-indexed values f_j exposed by (B5a,b) shows that the 2-periodic linear spline f interpolating (x_j, f_j) is fully determined, in the case $m = 11$, $n = 4$, by the odd-indexed values f_j, $j = 1, 3, \ldots, 11$, alone; see figure 22. This property generalizes to other pairs (m, n) with m and n of opposite parities, with the linear spline completely determined by the set of values f_j such that j has the same parity as m.

The inconsistency of the system (4.14) when $r = m/n$ with both m and n odd is argued in §4.2 for the case $m = n = 1$. For completeness, it is also illustrated here for $m = 5$ and

$n = 3$. The system

$$
\begin{bmatrix}
1 & & & & \\
& 1 & & & \\
& & 1 & & \\
& & & 1 & \\
& & & & 1
\end{bmatrix}
\begin{bmatrix}
1 & & & \\
& 1 & & \\
& & 1 & \\
& & & 1 \\
& & & & 1
\end{bmatrix}
\begin{bmatrix}
f_{-2} \\ f_{-1} \\ f_0 \\ \hline f_1 \\ f_2 \\ f_3 \\ f_4 \\ f_5 \\ \hline f_6 \\ f_7 \\ f_8 \\ f_9
\end{bmatrix}
= 2
\begin{bmatrix}
x_1 \\ x_2 \\ x_3 \\ x_4 \\ x_5
\end{bmatrix}
\tag{B6}
$$

for $f_j = f(x_j)$ at $x_j = j/10$ is similar to (B1), and now folds into the system

$$
\boldsymbol{A}f(x) =
\begin{bmatrix}
-1 & & & 1 \\
-1 & & 1 & \\
& & 1 & \\
1 & 1 & & \\
1 & 1 & &
\end{bmatrix}
\begin{bmatrix}
f_1 \\ f_2 \\ f_3 \\ f_4 \\ f_5
\end{bmatrix}
= 2
\begin{bmatrix}
x_1 \\ x_2 \\ x_3 \\ x_4 \\ x_5
\end{bmatrix},
\tag{B7}
$$

using the parity conditions $f_{-j} = -f_j$, $j = 0, 1, 2$, and symmetries $f_{5+j} = f_{5-j}$, $j = 1, 2, 3, 4$. The system (B7) is inconsistent, in view of its last two equations. In this case alternative **A1** fails and alternative **A2** holds, leading to a resonant response.

Appendix C. Proof of (4.20)

For $r = 1 - 1/m$ with $m > 1$ (i.e. $n = m - 1$), the system (4.14) becomes

$$
\begin{bmatrix}
& & & -1 & 0 & 1 \\
& & \cdot^{\cdot^{\cdot}} & \cdot^{\cdot^{\cdot}} & \cdot^{\cdot^{\cdot}} & \\
& \cdot^{\cdot^{\cdot}} & \cdot^{\cdot^{\cdot}} & \cdot^{\cdot^{\cdot}} & & \\
-1 & 0 & 1 & & & \\
0 & 1 & & & & \\
2 & & & & &
\end{bmatrix}
\begin{bmatrix}
f_1 \\ \vdots \\ \vdots \\ f_{m-2} \\ f_{m-1} \\ f_m
\end{bmatrix}
= 2
\begin{bmatrix}
x_1 \\ \vdots \\ \vdots \\ x_{m-2} \\ x_{m-1} \\ x_m
\end{bmatrix},
\tag{C1}
$$

with $x_j = j/(2m)$, $f_j = f(x_j)$, $j = 1, \ldots, m$ and $f = f_{1-1/m}$; see Appendix B for the construction of this system. This system is easily solved via backward substitution, i.e.

$$
f_j = j/2 - \lfloor j/2 \rfloor \lceil j/2 \rceil / m, \quad j = 1, \ldots, m,
\tag{C2}
$$

where $\lfloor \cdot \rfloor$ and $\lceil \cdot \rceil$ denote the floor and ceiling functions (functions which take a real argument and return the greatest/least integer less/greater than or equal to the argument, respectively). In particular, the maximal value over all j is obtained for $j = m$ at $x_m = 0.5$,

$$
f_m = m/2 - \lfloor m/2 \rfloor \lceil m/2 \rceil / m = m/4 +
\begin{cases}
0 & \text{if } m \text{ even,} \\
1/(4m) & \text{if } m \text{ odd.}
\end{cases}
\tag{C3}
$$

For $j = j(m)$ such that $x_j \to x \in [0, 0.5]$ as $m \to \infty$, $\lfloor j/2 \rfloor / m \to x$, $\lceil j/2 \rceil / m \to x$ and

$$
f_j/(m/4) = 4x_j - 4(\lfloor j/2 \rfloor / m)(\lceil j/2 \rceil / m) \to 4x - 4x^2 = 4x(1 - x),
\tag{C4}
$$

so that $f_j/f_m \to 4x(1-x)$ as well. Using $f(-x) = -f(x)$ and $f(0.5 + x) = f(0.5 - x)$ for $|x| \le 0.5 - 1/(2m)$ shows that, in the limit $m \to \infty$, f satisfies (4.20).

915 A85-40

The right-hand side function of (4.20) is the quadratic Euler spline $S_2(x - 0.5)$ (Olver *et al.* 2010, equation 24.17.3). The first $m - 1$ equations in the system (C1) can then be interpreted as a central-finite-difference discretization of the boundary value problem

$$\tilde{f}'(x) = S_2'(x) = 4 - 8x, \quad 0 < x < 0.5, \quad \tilde{f}(0) = 0, \tag{C5}$$

for the scaled function $\tilde{f} = (4/m)f$. The last equation corresponds to an odd parity condition at 0.

Appendix D. Proof that (4.21) is odd and satisfies (4.10) and (4.13) when m and n are odd and f_1 is 1-antiperiodic

The odd parity of $f_{n/m}$ defined by (4.21) follows from that of f_1. Next, note that the 1-antiperiodicity of f_1 implies that it satisfies (4.13) for all x, not just $|x| \leq 0.5$. Then, for $m = 2m' + 1$ an odd integer,

$$f_{n/m}(0.5 + x) = f_1(m/2 + mx) = (-1)^{m'} f_1(0.5 + mx)$$
$$= (-1)^{m'} f_1(0.5 - mx) = f_1(m/2 - mx) = f_{n/m}(0.5 - x), \tag{D1}$$

for all real x. Similarly, for $n = 2n' + 1$ an odd integer,

$$f_{n/m}(n/(2m) + x) = f_1(n/2 + mx) = (-1)^{n'} f_1(0.5 + mx) = (-1)^{n'} f_1(0.5 - mx)$$
$$= f_1(n/2 - mx) = f_{n/m}(n/(2m) - x). \tag{D2}$$

Assuming that f_1 is a 1-antiperiodic (i.e. extended outside the interval $[-1, 1]$) simplifies the above proof and removes a technicality associated with the range $[-(m + n)/2, (m + n)/2]$ of mx values which (4.21) requires in order to be able to evaluate the associated mode everywhere in the cavity.

Appendix E. Determination of the coefficients a_j in (4.27)

The existence of the representation (4.27) follows from the full characterization of the linear spline f from its values f_{2j-1} at $\zeta_j = (2j - 1)/(2m) = x_{2j-1}$, as illustrated in Appendix B. From the expression $S_1(\zeta) = 1 - 2|\zeta|$ for $|\zeta| \leq 1$, for $k = 1, \ldots, m$, we obtain

$$-f_{2k-3} + 2f_{2k-1} - f_{2k+1} = \sum_{j=1}^{m} a_j[-S_1(\zeta_{k-1} - \zeta_j) + 2S_1(\zeta_k - \zeta_j) - S_1(\zeta_{k+1} - \zeta_j)]$$

$$= 2\sum_{j=1}^{m} a_j[|\zeta_{k-1} - \zeta_j| - 2|\zeta_k - \zeta_j| + |\zeta_{k+1} - \zeta_j|]$$

$$= 2a_k[|\zeta_{k-1} - \zeta_k| + |\zeta_{k+1} - \zeta_j|] = \frac{4}{m}a_k. \tag{E1}$$

For $k = 1$ and m, we use the symmetries $f_{-1} = -f_1$ and $f_{2m+1} = -f_{2m-1}$ to get the relations $3f_1 - f_3 = 4a_1/m$ and $-f_{2m-3} + 3f_{2m-1} = 4a_m/m$. Thus,

$$\begin{bmatrix} 3 & -1 & & & \\ -1 & 2 & -1 & & \\ & \ddots & \ddots & \ddots & \\ & & -1 & 2 & -1 \\ & & & -1 & 3 \end{bmatrix} \begin{bmatrix} f_1 \\ f_3 \\ \vdots \\ f_{2m-3} \\ f_{2m-1} \end{bmatrix} = \frac{4}{m} \begin{bmatrix} a_1 \\ a_2 \\ \vdots \\ a_{m-1} \\ a_m \end{bmatrix}. \tag{E2}$$
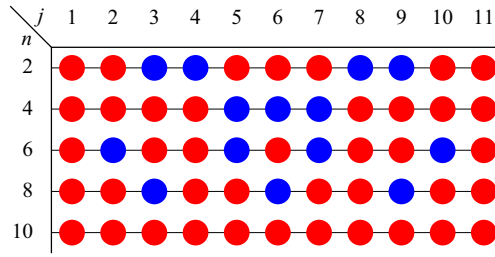
Figure 23. Signs of coefficients a_j for $m = 11$ and n and j as indicated; blue is negative and red is positive.

The symmetry $f_{2m-k} = f_k$ for $k = 1, 3, \ldots, 2m - 1$ implies that $a_{m-j} = a_j$ for $j = 1, \ldots, m - 1$. It also makes it possible to halve the size of (E2) by only considering the first $m' = \lceil m/2 \rceil$ coefficients, i.e.

$$
\begin{bmatrix}
3 & -1 & & & \\
-1 & 2 & -1 & & \\
& \ddots & \ddots & \ddots & \\
& & -1 & 2 & -1 \\
& & & -2 & 2
\end{bmatrix}
\begin{bmatrix}
f_1 \\
f_3 \\
\vdots \\
f_{2m'-3} \\
f_{2m'-1}
\end{bmatrix}
= \frac{4}{m}
\begin{bmatrix}
a_1 \\
a_2 \\
\vdots \\
a_{m'-1} \\
a_{m'}
\end{bmatrix}. \tag{E3}
$$

The matrices in (E2) and (E3) play a fundamental role in the theory of discrete sine transforms, introduced as alternatives to the discrete Fourier transform for data with specific symmetries (Britanak *et al.* (2007), page 36). For the example with $m = 11$ and $n = 4$ used in Appendix B, we obtain $m' = 6$ and

$$
\begin{bmatrix}
a_1 \\
a_2 \\
a_3 \\
a_4 \\
a_5 \\
a_6
\end{bmatrix}
= \frac{11}{4}
\begin{bmatrix}
3 & -1 & & & & \\
-1 & 2 & -1 & & & \\
& -1 & 2 & -1 & & \\
& & -1 & 2 & -1 & \\
& & & -1 & 2 & -1 \\
& & & & -2 & 2
\end{bmatrix}
\frac{1}{22}
\begin{bmatrix}
5 \\
11 \\
13 \\
11 \\
5 \\
3
\end{bmatrix}
= \frac{1}{2}
\begin{bmatrix}
1 \\
1 \\
1 \\
1 \\
-1 \\
-1
\end{bmatrix},
$$

$$
\begin{bmatrix}
a_7 \\
a_8 \\
a_9 \\
a_{10} \\
a_{11}
\end{bmatrix}
=
\begin{bmatrix}
a_5 \\
a_4 \\
a_3 \\
a_2 \\
a_1
\end{bmatrix}
= \frac{1}{2}
\begin{bmatrix}
-1 \\
1 \\
1 \\
1 \\
1
\end{bmatrix}. \tag{E4a,b}
$$

The fact that $a_j = \pm 0.5$ can be verified to hold for any m and n with opposite parities. The $\pm$ sign pattern is, in view of (E1), directly connected to the convexity of f, but its dependence on j and n for a fixed m is not immediately obvious. Figure 23 illustrates the patterns when $m = 11$. For the case $n = m - 1 = 10$ considered in Appendix C, $a_j = +0.5$ for all j. This remains true for other values of m. In particular,

$$
\frac{2}{m} f_{1-1/m}(\zeta) = \frac{1}{m} \sum_{j=1}^{m} S_1(\zeta - \zeta_j) \xrightarrow[\substack{\text{midpoint} \\ \text{rule}}]{m \to \infty} \int_0^1 S_1(\zeta - x) \mathrm{d}x = \int_{\zeta-1}^{\zeta} S_1(x) \mathrm{d}x = 2\zeta(1-\zeta) \tag{E5}
$$

for $0 \le \zeta \le 1$ shows that $f_{1-1/m}(\zeta) \sim (m/4)4\zeta(1-\zeta)$ grows with m as $m/4$ but its shape converges to $S_2(\zeta - 0.5)$ from figure 10, providing an alternate proof of (4.20).
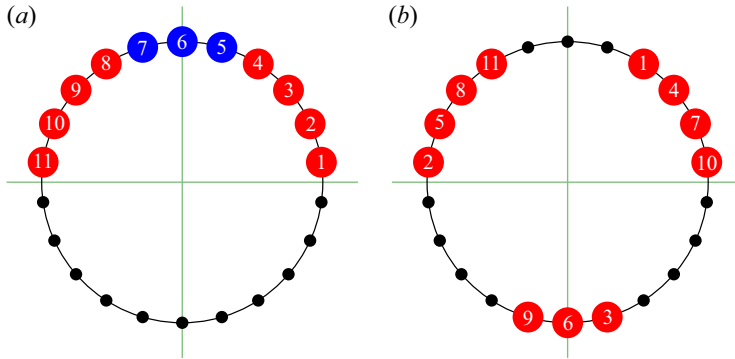
915 A85-42

Figure 24. (*a*) Signed complex numbers $2a_j \exp[i(2j-1)\pi/(2m)]$ for $j = 1, \ldots, m$ with $m = 11$. The blue and red nodes correspond to $2a_j = -1$ and $2a_j = 1$, respectively, for the $n = 4$ case from figure 23. The nodes are labelled by the value of j in the sum (F2). (*b*) The blue terms $-\exp[i(2j-1)\pi/(2m)]$ ($j = 5, 6, 7$) from (*a*) are replaced by a red conjugate $\exp[-i(2j-1)\pi/(2m)]$ and the label in the nodes now represents the value of the counter ℓ in the sum (F3). Nodes with successive labels are obtained via multiplication by $\xi = \exp[i(m-n)\pi/m]$, corresponding to a counter-clockwise turn by an angle equal to $m - n = 7$ nodes, starting with $\xi^{1/2}$ (label 1).

Appendix F. Evaluation of the coefficients s_k from (4.29)

The symmetry $a_{m+1-j} = a_j$ for $j = 1, \ldots, m$ implies that $\sum_{j=1}^{m} a_j \cos((2k+1)\pi\zeta_j) = 0$. Thus,

$$is_k = \sum_{j=1}^{m} 2a_j \exp(i(2k+1)\pi\zeta_j). \tag{F1}$$

Replacing each exponential term of the sum associated with a factor $2a_j = -1$ by $e^{-i\pi\zeta_j}$ enables the interpretation of is_k/m as the arithmetic mean of complex numbers on the unit circle and leads to the expression

$$s_k = -i\sum_{j=1}^{m} \exp(i\,\mathrm{sign}(a_j)(2k+1)\pi\zeta_j), \tag{F2}$$

where $0 < \zeta_j = (2j-1)\pi/(2m) < \pi$. Upon relabelling, the sum (F2) can be reformulated as a geometric sum of powers of $\xi = \exp[i(2k+1)(m-n)\pi/m]$. The process is illustrated in figure 24 for $m = 11$, $n = 4$ and $k = 0$. We obtain, with $r = n/m$,

$$s_k = -i\sum_{\ell=1}^{m} \xi^{\ell-1/2} = -i\xi^{1/2}\frac{1-\xi^m}{1-\xi} = \frac{2i}{\xi^{1/2}-\xi^{-1/2}} = \csc\frac{(2k+1)}{2}\frac{(m-n)}{m}\pi$$

$$= (-1)^k \sec\frac{(2k+1)}{2}r\pi. \tag{F3}$$

Appendix G. The linear inviscid forced response as a superposition of C^∞ elementary responses, (4.32), and its modal limit at resonance

Let $\rho_k = (2k+1)\pi$ and $\lambda_k = \rho_k r/2$. The expansion (4.31) yields

$$f_r(x+rz) - f_r(x-rz) = 4 \sum_{k \geq 0} \frac{(-1)^k}{\rho_k^2} \frac{\sin \rho_k(x+rz) - \sin \rho_k(x-rz)}{\cos \lambda_k}$$

$$= 8 \sum_{k \geq 0} \frac{(-1)^k}{\rho_k^2} \frac{\cos \rho_k x \, \sin \rho_k rz}{\cos \lambda_k}, \tag{G1}$$

$$2x - f_r(x+rz) - f_r(x-rz)$$
$$= f_r(x+r/2) + f_r(x-r/2) - f_r(x+rz) - f_r(x-rz)$$
$$= 4 \sum_{k \geq 0} \frac{(-1)^k}{\rho_k^2} \frac{\sin \rho_k(x+r/2) + \sin \rho_k(x-r/2) - \sin \rho_k(x+rz) - \sin \rho_k(x-rz)}{\cos \lambda_k}$$
$$= 8 \sum_{k \geq 0} \frac{(-1)^k}{\rho_k^2} \sin \rho_k rx \left(1 - \frac{\cos \rho_k rz}{\cos \lambda_k} \right), \tag{G2}$$

and

$$2rxz - F_r(x+rz) + F_r(x-rz) = r \int_0^z [2x - f_r(x+r\zeta) - f_r(x-r\zeta)] \, d\zeta$$

$$= 8 \sum_{k \geq 0} \frac{(-1)^k}{\rho_k^2} \sin \rho_k x \left(rz - \frac{\sin \rho_k rz}{\rho_k \cos \lambda_k} \right). \tag{G3}$$

The response (4.15) of the linear inviscid forced system (4.1) can thus be written as a superposition

$$(u, w, p, \theta) = 4 \sum_{k \geq 0} \frac{(-1)^k}{\rho_k} (u_k, w_k, p_k, \theta_k) \tag{G4}$$

of fields

$$\left. \begin{aligned} \begin{bmatrix} u_k \\ w_k \end{bmatrix} &= \frac{2c_r\sigma_r}{\rho_k} \begin{bmatrix} \dfrac{r\cos \rho_k x \, \sin \rho_k rz}{\cos \lambda_k} \\ \sin \rho_k x \left(1 - \dfrac{\cos \rho_k rz}{\cos \lambda_k} \right) \end{bmatrix} \cos \sigma_r t \\ &= -\frac{\alpha}{\sigma_r} \begin{bmatrix} \dfrac{\cos \rho_k x}{\cos \lambda_k} \dfrac{\sin \rho_k rz}{\rho_k r}, \\ \dfrac{1}{r^2} \dfrac{\sin \rho_k x}{\rho_k} \left(1 - \dfrac{\cos \rho_k rz}{\cos \lambda_k} \right) \end{bmatrix} \cos \sigma_r t, \\ \begin{bmatrix} p_k \\ \theta_k \end{bmatrix} &= -\frac{2c_r}{\rho_k} \begin{bmatrix} \lambda_r \sin \rho_k x \left[rz - \dfrac{\sin \rho_k rz}{\rho_k \cos \lambda_k} \right] \\ \sin \rho_k x \left[1 - \dfrac{\cos \rho_k rz}{\cos \lambda_k} \right] \end{bmatrix} \sin \sigma_r t \\ &= \alpha \frac{\sin \rho_k x}{\rho_k} \begin{bmatrix} z - \dfrac{1}{\cos \lambda_k} \dfrac{\sin \rho_k rz}{\rho_k r} \\ \dfrac{1+r^2}{r^2} \left[1 - \dfrac{\cos \rho_k rz}{\cos \lambda_k} \right] \end{bmatrix} \sin \sigma_r t. \end{aligned} \right\} \tag{G5}$$

The fields $(u_k, w_k, p_k, \theta_k)$ can be verified to satisfy the forced linear system (4.33) as well as the boundary conditions $u_k = \partial_x \theta_k = 0$ at $x = \pm 0.5$, and $w_k = \theta_k = 0$ at $z = \pm 0.5$.

915 A85-44

The resulting vorticity field

$$\eta_k = \partial_z u_k - \partial_x w_k = \frac{\alpha}{r^2 \sigma_r} \cos \rho_k x \left[1 - (1 + r^2) \frac{\cos \rho_k r z}{\cos \lambda_k} \right] \cos \sigma_r t \qquad (G6)$$

is also used to evaluate the vorticity of partial sums of the series (4.32) in figure 13. The associated streamfunction

$$\psi_k = -\frac{\alpha}{\sigma_r} \frac{\cos \rho_k x}{(\rho_k r)^2} \left[1 - \frac{\cos \rho_k r z}{\cos \lambda_k} \right] \cos \sigma_r t \qquad (G7)$$

vanishes at all boundaries of the cavity. Its ρ_k^{-2} dependence on k makes the series (4.32) converge fast for the overall streamfunction ψ from (4.8).

The limit of (G5) as $r \to r^* = n/m$, with m and n both odd and $m \wedge n = 1$ (prime with each other), can be taken for values of k such that $\cos \lambda_k^* = 0$, where $\lambda_k^* = \rho_k r^*/2$. These are the sole contributors, at the limit, to the overall series (4.32). In this case, $(2k + 1)r^*$ is an odd integer. Since $m \wedge n = 1$, $2k + 1 = (2\ell + 1)m$ for $\ell \in \mathbb{N}$. Consequently, $\rho_k r^*/2 = 2\pi \ell(n-1)/2 + (\ell + (n-1)/2)\pi + \pi/2$ and

$$\cos \lambda_k = \cos[\lambda_k^* + (\lambda_k - \lambda_k^*)] = -\sin \lambda_k^* \sin(\lambda_k - \lambda_k^*) \approx -(-1)^{\ell+(n-1)/2} (\lambda_k - \lambda_k^*). \qquad (G8)$$

Thus, $\rho_k = (2\ell + 1)m\pi$, $\rho_k r^* = (2\ell + 1)n\pi$, and as $r \to r^*$,

$$\begin{bmatrix} u_k \\ w_k \end{bmatrix} \approx -\frac{\alpha}{\cos \lambda_k} \frac{1}{\rho_k r^{*2} \sigma_{r^*}} \begin{bmatrix} r^* \cos \rho_k x \sin \rho_k r^* z \\ -\sin \rho_k x \cos \rho_k r^* z \end{bmatrix} \cos \sigma_{r^*} t$$

$$\approx \gamma_k \sigma_{r^*} \begin{bmatrix} r^* \cos(2\ell + 1)m\pi x \sin(2\ell + 1)n\pi z \\ -\sin(2\ell + 1)m\pi x \cos(2\ell + 1)n\pi z, \end{bmatrix} \cos \sigma_{r^*} t, \qquad (G9a)$$

$$\begin{bmatrix} p_k \\ \theta_k \end{bmatrix} \approx -\frac{\alpha}{\cos \lambda_k} \frac{\sin \rho_k x}{\rho_k r^{*2}} \begin{bmatrix} \dfrac{r^*}{\rho_k} \sin \rho_k r^* z \\ (1 + r^{*2}) \cos \rho_k r^* z \end{bmatrix} \sin \sigma_{r^*} t$$

$$\approx \gamma_k \begin{bmatrix} \dfrac{r^* \sigma_{r^*}^2}{(2\ell + 1)m\pi} \sin(2\ell + 1)m\pi x \sin(2\ell + 1)n\pi z \\ \sin(2\ell + 1)m\pi x \cos(2\ell + 1)n\pi z \end{bmatrix} \sin \sigma_{r^*} t, \qquad (G9b)$$

where

$$\gamma_k = \frac{\alpha}{r - r^*} \frac{2(-1)^{\ell+(n-1)/2}}{\rho_k^2 r^{*2} \sigma_{r^*}^2} = \frac{\alpha}{r - r^*} \frac{2(-1)^{(n-1)/2}}{\pi^2} \left(\frac{1}{m^2} + \frac{1}{n^2} \right) \frac{(-1)^\ell}{(2\ell + 1)^2}. \qquad (G10)$$

The forced responses $R_{f_k} \approx \gamma_k I_k$, with components given by (G9) that are scaled versions of those in (4.25) of $I_k = I_{(2\ell+1)m:(2\ell+1)n}$, combine into the infinite sum (4.32),

$$R_f \approx \frac{4}{\pi} \sum_{k \geq 0} \frac{(-1)^k}{2k + 1} \gamma_k I_k$$

$$= \frac{\alpha}{r - r^*} \frac{8(-1)^{(n-1)/2}}{\pi^3} \left(\frac{1}{m^2} + \frac{1}{n^2} \right) \sum_{\ell \geq 0} \frac{(-1)^{\ell m+(m-1)/2}}{(2\ell + 1)m} \frac{(-1)^\ell}{(2\ell + 1)^2} I_{(2\ell+1)m:(2\ell+1)n}$$

$$= \mu_{r^*} \sum_{\ell \geq 0} \frac{1}{(2\ell + 1)^3} I_{(2\ell+1)m:(2\ell+1)n}, \qquad (G11)$$

using the fact that $\ell(m + 1)$ is an even integer, with

$$\mu_{r*}(r) = -\frac{8}{\pi^3}\frac{(-1)^{(m+n)/2}}{m}\left(\frac{1}{m^2} + \frac{1}{n^2}\right)\frac{\alpha}{r - r*}. \tag{G12}$$

Note that $\mu_{r*}(r) = -(1/r)\,\mu_{1/r*}(1/r)$, i.e. the resonant response is stronger for $r \approx r* < 1$ ($\omega^2 > 0.5$), which is consistent with the response diagram in figure 2(a).

The limiting process $r \to r*$ carried out directly on f_r from (4.31), using (G8), yields

$$f_r(\zeta) \approx -\frac{4}{\pi^2}\sum_{\ell \geq 0}\frac{(-1)^{\ell m + (m-1)/2}}{(2\ell + 1)^2\,m^2}\frac{\sin(2\ell + 1)m\pi\zeta}{(-1)^{\ell + (n-1)/2}(2\ell + 1)\,m\pi\,(r - r*)/2}$$

$$= -\frac{(-1)^{(m+n)/2}}{4m^3(r - r*)}\left(\frac{32}{\pi^3}\right)\sum_{\ell \geq 0}\frac{\sin(2\ell + 1)m\pi\zeta}{(2\ell + 1)^3} = -\frac{(-1)^{(m+n)/2}}{4m^3(r - r*)}S_2(m\zeta - 0.5), \tag{G13}$$

where $S_2(\cdot - 0.5)$ is the 1-antiperiodic quadratic spline shown in figure 10(b). For the case $m = 1$, one immediately recovers (4.20). Note that m in (4.20) is related to $r = 1 - 1/m$, while m here is related to the limiting value $r* = n/m$. Moreover, the scaling of (G13) reduces, in the case $n = 1$, to the factor $m/4$, with m as in (G13), already obtained in Appendix C.

Appendix H. Inviscid estimate of mean enstrophy

The inviscid enstrophy is determined by substituting the expression (G7) into the series (G4). The orthogonality

$$\int_{-0.5}^{0.5}\cos\rho_k x\cos\rho_\ell x\,\mathrm{d}x = 0, \quad k \neq \ell, \tag{H1}$$

implies that $\{\eta_k\}_{k \geq 0}$ forms an orthogonal sequence with respect to the $L_2([-0.5, 0.5]^2 \times [0, \tau])$ inner product. This yields

$$\langle\mathcal{E}\rangle_\tau = \frac{1}{\tau}\int_0^\tau\int_{-0.5}^{0.5}\int_{-0.5}^{0.5}\left[4\sum_{k \geq 0}(-1)^k\frac{\eta_k}{\rho_k}\right]^2\mathrm{d}x\,\mathrm{d}z = \frac{16}{\tau}\sum_{k \geq 0}\frac{1}{\rho_k^2}\int_0^\tau\int_{-0.5}^{0.5}\int_{-0.5}^{0.5}\eta_k^2\,\mathrm{d}x\,\mathrm{d}z$$

$$= \frac{16\alpha^2}{r^4\sigma_r^2}\sum_{k \geq 0}\frac{1}{\tau\rho_k^2}\int_0^\tau\cos^2\sigma_r t\,\mathrm{d}t\int_{-0.5}^{0.5}\cos^2\rho_k x\,\mathrm{d}x$$

$$\times\int_{-0.5}^{0.5}\left[1 - (1 + r^2)\frac{\cos\rho_k rz}{\cos\lambda_k}\right]^2\mathrm{d}x\,\mathrm{d}z$$

915 A85-46

$$= \frac{4\alpha^2}{r^4\sigma_r^2} \sum_{k \geq 0} \rho_k^{-2} \left\{ 1 - 4(1 + r^2)\frac{\sin(\lambda_k)/(\rho_k r)}{\cos\lambda_k} + (1 + r^2)^2\frac{1 + \sin(\rho_k r)/(\rho_k r)}{2\cos^2\lambda_k} \right\}$$

$$= \frac{\alpha^2}{r^2\sigma_r^2} \sum_{k \geq 0} \lambda_k^{-2} \left\{ 1 + \frac{1 + r^2}{2}\left[(1 + r^2)\sec^2\lambda_k - (3 - r^2)\frac{\tan\lambda_k}{\lambda_k} \right] \right\}. \tag{H2}$$

Note that, for fixed k, the term in the curly brackets is $O(r^4)$ as $r \to 0$ ($\omega = \sigma_r \to 1$).

REFERENCES

ALDRIDGE, K.D. 1975 Inertial waves and the Earth's outer core. *Geophys. J. R. Astron. Soc.* **42**, 337–345.

ALDRIDGE, K.D. & TOOMRE, A. 1969 Axisymmetric inertial oscillations of a fluid in a rotating spherical container. *J. Fluid Mech.* **37**, 307–323.

BAJARS, J., FRANK, J. & MAAS, L.R.M. 2013 On the appearance of internal wave attractors due to an initial or parametrically excited disturbance. *J. Fluid Mech.* **714**, 283–311.

BECKEBANZE, F. 2015 On functional equations leading to analytical solutions of internal waves. Master's thesis, Utrecht University.

BECKEBANZE, F. & KEADY, G. 2016 On functional equations leading to exact solutions for standing internal waves. *Wave Motion* **60**, 181–195.

BENIELLI, D. & SOMMERIA, J. 1998 Excitation and breaking of internal gravity waves by parametric instability. *J. Fluid Mech.* **374**, 117–144.

BENJAMIN, T.B. & URSELL, F. 1954 The stability of the plane free surface of a liquid in vertical periodic motion. *Proc. R. Soc. Lond.* A **225**, 505–515.

BORCIA, I.D., ABOUZAR, G.V. & HARLANDER, U. 2014 Inertial wave mode excitation in a rotating annulus with partially librating boundaries. *Fluid Dyn. Res.* **46**, 041423.

BOURY, S., PEACOCK, T. & ODIER, P. 2019 Excitation and resonant enhancement of axisymmetric internal wave modes. *Phys. Rev. Fluids* **4**, 034802.

BRITANAK, V., YIP, P.C. & RAO, K.R. (Eds) 2007 *Discrete Cosine and Sine Transforms*. Academic Press.

DAUXOIS, T., JOUBAUD, S., ODIER, P. & VENAILLE, A. 2018 Instabilities of internal gravity wave beams. *Annu. Rev. Fluid Mech.* **50**, 1–28.

DELHEZ, E.J.M. & DELEERSNIJDER, E. 2007 Overshootings and spurious oscillations caused by biharmonic mixing. *Ocean Model.* **17**, 183–198.

FARADAY, M. 1831 On a peculiar class of acoustical figures; and on certain forms assumed by groups of particles upon vibrating elastic surfaces. *Phil. Trans. R. Soc.* A **121**, 299–340.

GAPONENKO, Y.A., TORREGROSA, M., YASNOU, V., MIALDUN, A. & SHEVTSOVA, V. 2015 Dynamics of the interface between miscible liquids subjected to horizontal vibration. *J. Fluid Mech.* **784**, 342–372.

GÖRTLER, H. 1943 Über eine Schwingungserscheinung in Flüssigkeiten mit stabiler Dichteschichtung. *Z. Angew. Math. Mech.* **23**, 65–71.

GRAYER, H., YALIM, J., WELFERT, B.D. & LOPEZ, J.M. 2020 Dynamics in a stably stratified tilted square cavity. *J. Fluid Mech.* **883**, A62.

GRÉA, B.-J. & BRIARD, A. 2019 Frozen waves in turbulent mixing layers. *Phys. Rev. Fluids* **4**, 064608.

GREENSPAN, H.P. 1965 On the general theory of contained rotating fluid motions. *J. Fluid Mech.* **22**, 449–462.

GRIFFIES, S.M. 2004 *Fundamentals of Ocean Climate Models*. Princeton University Press.

HALE, J.K. 2009 *Ordinary Differential Equations*. Dover Publications.

HARLANDER, U. & MAAS, L.R.M. 2007 Two alternatives for solving hyperbolic boundary value problems of geophysical fluid dynamics. *J. Fluid Mech.* **588**, 331–351.

JALIKOP, S.V. & JUEL, A. 2009 Steep capillary-gravity waves in oscillatory shear-driven flows. *J. Fluid Mech.* **640**, 131–150.

KELLER, J.B. & TING, L. 1966 Periodic vibrations of systems governed by nonlinear partial differential equations. *Commun. Pure Appl. Maths* **19**, 371–420.

KELVIN, LORD 1880 Vibrations of a columnar vortex. *Phil. Mag.* **10**, 155–168.

KUCZMA, M., CHOCZEWSKI, B. & GER, R. (Eds) 1990 *Iterative Functional Equations*. Cambridge University Press.

KUMAR, K. & TUCKERMAN, L.S. 1994 Parametric instability of the interface between two fluids. *J. Fluid Mech.* **279**, 49–68.

LALÍN, M., RODRIGUE, F. & ROGERS, M. 2014 Secant Zeta functions. *J. Math. Anal. Appl.* **409**, 197–204.

LE BARS, M., CEBRON, D. & LE GAL, P. 2015 Flows driven by libration, precession, and tides. *Annu. Rev. Fluid Mech.* **47**, 163–193.

MAAS, L.R.M. 2003 On the amphidromic structure of inertial waves in a rectangular parallelepiped. *Fluid Dyn. Res.* **33**, 373–401.

MAAS, L.R.M. & LAM, F.-P.A. 1995 Geometric focusing of internal waves. *J. Fluid Mech.* **300**, 1–41.

MANTON, M.J. & MYSAK, L.A. 1971 Construction of internal wave solutions via a certain functional equation. *J. Math. Anal. Appl.* **35**, 237–248.

MCEWAN, A.D. 1971 Degeneration of resonantly-excited standing internal gravity waves. *J. Fluid Mech.* **50**, 431–448.

MERCIER, M.J., MARTINAND, D., MATHUR, M., GOSTIAUX, L., PEACOCK, T. & DAUXOIS, T. 2010 New wave generation. *J. Fluid Mech.* **657**, 308–334.

MILES, J. & HENDERSON, D.M. 1990 Parametrically forced surface-waves. *Annu. Rev. Fluid Mech.* **22**, 143–165.

MOWBRAY, D.E. & RARITY, B.S.H. 1967 A theoretical and experimental investigation of the phase configuration of internal waves of small amplitude in a density stratified liquid. *J. Fluid Mech.* **28**, 1–16.

OLVER, F.W.J., LOZIER, D.W., BOISVERT, R.F. & CLARK, C.W. (Eds) 2010 *NIST Handbook of Mathematical Functions*. Cambridge University Press.

PILLET, G., ERMANYUK, E.V., MAAS, L.R.M., SIBGATULLIN, I.N. & DAUXOIS, T. 2018 Internal wave attractors in three-dimensional geometries: trapping by oblique reflection. *J. Fluid Mech.* **845**, 203–225.

PILLET, G., MAAS, L.R.M. & DAUXOIS, T. 2019 Internal wave attractors in 3D geometries: a dynamical systems approach. *Eur. J. Mech. B/Fluids* **77**, 1–16.

POINCARÉ, H. 1885 Sur l'équilibre d'une masse fluide animée d'un mouvement de rotation. *Acta Mathematica* **7**, 259–380.

RICHTER, S. & BESTEHORN, M. 2019 Direct numerical simulations of liquid films in two dimensions under horizontal and vertical external vibrations. *Phys. Rev. Fluids* **4**, 044004.

RIEUTORD, M., GEORGEOT, B. & VALDETTARO, L. 2000 Wave attractors in rotating fluids: a paradigm for ill-posed Cauchy problems. *Phys. Rev. Lett.* **85**, 4277–4280.

RIEUTORD, M. & VALDETTARO, L. 2018 Axisymmetric inertial modes in a spherical shell at low Ekman numbers. *J. Fluid Mech.* **844**, 597–634.

RILEY, J.J. & LELONG, M.-P. 2000 Fluid motions in the presence of strong stable stratification. *Annu. Rev. Fluid Mech.* **32**, 613–657.

SAVARO, C., CAMPAGNE, A., LINARES, M.C., AUGIER, P., SOMMERIA, J., VALRAN, T., VIBOUD, S. & MORDANT, N. 2020 Generation of weakly nonlinear turbulence of internal gravity waves in the Coriolis facility. *Phys. Rev. Fluids* **5**, 073801.

SCHOENBERG, I.J. 1973 *Cardinal Spline Interpolation*. SIAM.

SHEVTSOVA, V., GAPONENKO, Y.A., YASNOU, V., MIALDUN, A. & NEPOMNYASHCHY, A. 2016 Two-scale wave patterns on a periodically excited miscible liquid–liquid interface. *J. Fluid Mech.* **795**, 409–422.

STAQUET, C. & SOMMERIA, J. 2002 Internal gravity waves: from instabilities to turbulence. *Annu. Rev. Fluid Mech.* **34**, 559–593.

SWART, A., SLEIJPEN, G.L.G., MAAS, L.R.M. & BRANDTS, J. 2007 Numerical solution of the two-dimensional Poincaré equation. *J. Comput. Appl. Maths* **200**, 317–341.

TADMOR, E. 2007 Filters, mollifiers and the computation of the Gibbs phenomenon. *Acta Numerica* **16**, 305–378.

TALIB, E., JALIKOP, S.V. & JUEL, A. 2007 The influence of viscosity on the frozen wave instability: theory and experiment. *J. Fluid Mech.* **584**, 45–68.

THORPE, S.A. 1968 On standing internal gravity waves of finite amplitude. *J. Fluid Mech.* **32**, 489–528.

TURNER, J.S. 1979 *Buoyancy Effects in Fluids*. Cambridge University Press.

VOISIN, B. 2003 Limit states of internal wave beams. *J. Fluid Mech.* **496**, 243–293.

WELFERT, B.D. 2020 The second secant zeta function and its anti-periodization evaluated at $1/\sqrt{n}$. arXiv:2007.12321.

WOLF, G.H. 1969 The dynamic stabilization of the Rayleigh–Taylor instability and the corresponding dynamic equilibrium. *Z. Phys.* A **227**, 291–300.

WOLF, G.H. 1970 Dynamic stabilization of the interchange instability of a liquid–gas interface. *Phys. Rev. Lett.* **24**, 444–446.

WOTHERSPOON, S. 1995 Internal tides and resonance. PhD thesis, University of Tasmania, Australia.

WU, K., WELFERT, B.D. & LOPEZ, J.M. 2018a Complex dynamics in a stratified lid-driven square cavity flow. *J. Fluid Mech.* **855**, 43–66.

WU, K., WELFERT, B.D. & LOPEZ, J.M. 2018b Librational forcing of a rapidly rotating fluid-filled cube. *J. Fluid Mech.* **842**, 469–494.

WU, K., WELFERT, B.D. & LOPEZ, J.M. 2020 Reflections and focusing of inertial waves in a librating cube with the rotation axis oblique to its faces. *J. Fluid Mech.* **896**, A5.

WUNENBURGER, R., EVESQUE, P., CHABOT, C., GARRABOS, Y., FAUVE, S. & BEYSENS, D. 1999 Frozen wave induced by high frequency horizontal vibrations on a CO_2 liquid–gas interface near the critical point. *Phys. Rev.* E **59**, 5440–5445.

YALIM, J., LOPEZ, J.M. & WELFERT, B.D. 2018 Vertically forced stably stratified cavity flow: instabilities of the basic state. *J. Fluid Mech.* **851**, R6.

YALIM, J., LOPEZ, J.M. & WELFERT, B.D. 2020 Parametrically forced stably stratified flow in a three-dimensional rectangular container. *J. Fluid Mech.* **900**, R3.

YALIM, J., WELFERT, B.D. & LOPEZ, J.M. 2019a Modal reduction of a parametrically forced confined viscous flow. *Phys. Rev. Fluids* **4**, 103903.

YALIM, J., WELFERT, B.D. & LOPEZ, J.M. 2019b Parametrically forced stably stratified cavity flow: complicated nonlinear dynamics near the onset of instability. *J. Fluid Mech.* **871**, 1067–1096.